

A multiphase model for compressible granular–gaseous flows: formulation and initial tests

Ryan W. Houim^{1,†} and Elaine S. Oran¹

¹Department of Aerospace Engineering, University of Maryland, College Park, MD 20742, USA

(Received 19 June 2015; revised 28 October 2015; accepted 7 December 2015;
first published online 18 January 2016)

A model for predicting the behaviour of a compressible flow laden with shocks interacting with granular material has been developed and tested. The model consists of two sets of coupled Euler equations, one for the gas phase and the other for the granular phase. Drag, convective, heat transfer and non-conservative terms couple the two sets of governing equations. Intergranular stress acting on the grains is modelled using granular kinetic theory in dilute regimes where particle collisions are dominant and frictional–collisional pressure in dense regions where layers of granular material slide over one another. The two-phase granular–gaseous model, as a result, is valid from dilute to densely packed granular regimes. The solution of these nonlinearly coupled Euler equations is challenging due to the presence of the non-conservative nozzling and work terms. A numerical technique, based on Godunov’s method, was designed for solving these equations. This method takes advantage of particle incompressibility to simplify the nozzling terms. It also uses the observation that a Riemann problem is valid in the region where gas can flow between particles and can be used to provide a physically accurate approximation of the non-conservative terms. The model and solution method are verified by comparisons to test problems involving granular shocks and two-phase shock-tube problems, and they are validated against experimental measurements of shock and dense particle-curtain interactions and transmitted oblique granular shocks.

Key words: granular media, multiphase flow, shock waves

1. Introduction

A granular fluid describes a collection of discrete, solid, macroscopic particles that collide and interact through energy-loss mechanisms, such as friction and inelastic collisions. As such, granular fluids are dissipative systems. The particles are large enough so that, unlike molecules and smaller nano-sized particles (Talbot *et al.* 1980), they are not affected by thermal fluctuations. The lower size limit for particles in a granular fluid is usually assumed to be of the order of a micrometre (Andreotti, Forterre & Pouliquen 2013). There does not appear to be an upper size limit as long as the number of interacting particles is large enough.

[†] Email address for correspondence: rhouim@umd.edu

Granular fluids and gaseous fluids differ in important ways. Collisions among granular particles are inelastic, unlike molecular gases, in which collisions are almost always fully elastic. These inelastic particle collisions can lead to granular clustering because, with inelastic collisions, the relative motion between the particles decreases (Brilliantov & Pöschel 2004). This can lead to behaviour where a ‘Maxwell’s demon’ effectively operates in granular systems. For example, particles in a shaken box may cluster to one side, leaving the other side evacuated (Van der Weele 2008). Granular media can also behave like a gas, liquid or solid depending on how the particles are packed and the amount of kinetic energy input. Understanding and developing models for many of the interesting phenomena related to granular media are now heavily researched topics.

In the past, efforts were made to develop models for the multiphase flow of coupled gas and granular fluids because of their importance for practical problems, such as coal combustors (Zhou *et al.* 2011), catalytic bed reactors (Zimmermann & Taghipour 2005), biomass gasification (Gerber, Behrendt & Oevermann 2010), particle hoppers (Srivastava & Sundaresan 2003), scouring sand underneath submerged pipes (Zhao & Fernando 2007) and pyroclastic flows (Neri *et al.* 2003). A number of methods have been developed to study these essentially low-speed incompressible flow problems (as described in § 2).

High-speed, compressible, dense granular multiphase flows occur in a wide range of scenarios, including dust explosions in coal mines (Sapko *et al.* 2000; Zheng *et al.* 2009), grain elevators, food processing and storage facilities, volcanic eruptions (Wilson 1980), dust layers lifted by shocks (Zydak & Klemens 2007; Chuanjie *et al.* 2012; Wayne *et al.* 2013), dust in natural gas explosions (Liu *et al.* 2013) and interior ballistics (Koo & Kuo 1977; Markatos & Kirkcaldy 1983; Markatos 1986; Porterie & Loraud 1994; Nussbaum *et al.* 2006). Although these are extremely important problems, much less work has been done to formulate models that consistently cover the range from dilute to dense particle packing in the presence of high-speed gas flows and shock waves. There are a few notable exceptions, such as the models by Fan *et al.* (2007), Chuanjie *et al.* (2012) and Khmel’ & Fedorov (2015).

Consider an example of where high-speed compressible granular multiphase flows are important, that of layered coal-dust explosions (Houim & Oran 2015a,b). Here we are interested in knowing the behaviour of particles and their interactions with a high-speed background flow. This flow can sweep up and entrain particles that are initially in densely packed layers and then distribute these particles as a diluted mixture of particles and gas. Such flows may be highly turbulent and laden with shocks. To further complicate matters, the particles may react chemically, agglomerate or fragment (Dacombe *et al.* 1999). We need to know the controlling physical processes in such scenarios and how they affect the particle distribution and background flow. To achieve this, we need a model for a granular flow that interacts with a compressible background gas. This model must include enough of the physics for the background gas, the granular media and the coupling interactions between them to provide physically accurate predictions over a wide range of granular packing and background flow conditions.

Solving for the behaviour of such complex, heterogeneous flows is difficult because it is necessary to formulate a model that includes enough of the physics of a compressible gas, the particles and the interactions among these, and to develop numerical procedures that will handle inherent difficulties in solving this coupled model. In this paper, we first describe such a model and a solution approach that gives reasonable results when compared to theoretical limits and experiments, and so it is a start for solving the problems of coupled compressible flows with gas and granular material.

2. Background

One type of multiphase model for coupled gas and granular flows is described by a set of equations based on the kinetic theory of granular flow (Lun *et al.* 1984; Gidaspow 1994). These models describe the interaction of a molecular gas with an inelastic granular fluid (Brilliantov & Pöschel 2004) made up of many incompressible particles. In this type of formulation, granular fluids are characterized by a granular temperature (Θ_s), representing the random translational kinetic energy of the particles. The granular temperature is used in constitutive relations to compute a ‘solids pressure’ (p_s) that describes an intergranular stress resulting from particle collisions. The solids pressure for the granular phase is analogous to the usual pressure for the gas phase. Friction forces between colliding particles can become substantial when the volume fraction of particles (α_s) is high, which results in a large frictional–collisional pressure (p_{fric}) (Johnson & Jackson 1987). This type of granular–gas multiphase fluid model can be considered as a two-fluid model (Ishii & Hibiki 2006). There are many methods for solving these equations for low-speed flows, as reviewed in Van Wachem *et al.* (2001). There are now several existing numerical codes for simulating low-speed granular multiphase flows (such as MFIX (Syamlal, Rogers & O’Brien 1993)).

Many compressible granular multiphase flows are modelled using the ‘dust–gas approximation’, which neglects particle–particle interactions and collision processes, and so it effectively assumes that the particles are dilute in the background gas (Collins *et al.* 1994; Benkiewicz & Hayashi 2002; Saito, Marumoto & Takayama 2003; Pelanti & LeVeque 2006; Fedorov, Kharlamova & Khmel’ 2007; Kuhl, Bell & Beckner 2010). These models have been used to study detonations of particle suspensions, explosion suppression from aerosolized particles, lifting of dilute dust layers, and the dispersion and combustion of aluminium particles in the turbulent flow field generated by an explosion. They are not applicable when there are dense particle clusters, which could occur when dense dust layers are lifted by shocks (Fan *et al.* 2007), or in coalmine explosions, where settled layers of dust may accumulate to volume fractions of the order of 47 % (Edwards & Ford 1988). When the dust is dense, the effects of particle–particle interactions must be included.

When the volume fraction of particles is very high, it becomes necessary to use other types of models, such as the Baer–Nunziato (BN) equations (Baer & Nunziato 1986), the Nigmatulin equations (Nigmatulin 1990) or Eulerian interior ballistic models (Koo & Kuo 1977; Markatos & Kirkcaldy 1983; Markatos 1986; Porterie & Loraud 1994; Nussbaum *et al.* 2006). The BN equations were developed to describe high-pressure combustion processes, such as detonation of high-explosive charges, where particle compression and distortion are significant. The BN equations are a variant of the ‘seven-equation model’ presented by Saurel & Abgrall (1999), in which the interfacial velocity and pressure are chosen to be the particle velocity and gas-phase pressure, respectively. The BN model relaxes the particle incompressibility assumption used in the kinetic-theory approach mentioned above, but adds an advection equation for the solid volume fraction. Neglecting phase change, this equation is often written as

$$\frac{\partial \alpha_s}{\partial t} + \mathbf{v}_s \cdot \nabla \alpha_s = 0, \quad (2.1)$$

where α_s and \mathbf{v}_s are the volume fraction and velocity vector for the solid-phase particles, respectively. This new equation is written in a non-conservative form, and, as such, changes the physical nature of compression waves in the solid phase from

that predicted by kinetic-theory models. That is, granular-phase compression waves in the BN equations represent pressure waves moving through the solid material itself and, as a result, the volume fraction changes only at solid contact surfaces. The volume fraction equation for kinetic-theory-based models (assuming constant particle density and neglecting phase change) is

$$\frac{\partial \alpha_s}{\partial t} + \nabla \cdot \alpha_s \mathbf{v}_s = 0, \quad (2.2)$$

which has very different wave propagation properties from the volume fraction equation for BN models. Granular-phase compression waves for kinetic-theory-based models are produced by particle collisions that create compaction waves and granular shocks (Kamenetsky *et al.* 2000). These granular compaction waves and shocks, in turn, change the volume fraction of particles rather than the material density of the particles themselves. The BN equations, as a result, are more appropriate for highly packed (i.e. the particle volume fraction is at or above the random close-packing limit) granular mixtures at high pressures with constant compressive contact between the grains (Lhuillier, Chang & Theofanous 2013). Therefore, the use of BN-type models is physically inappropriate for looser granular flow regimes, where the particles are not in constant compressive contact and intergranular stress results from collisions and friction between the grains, which are the focus of this paper.

Interior gun ballistic models (Koo & Kuo 1977; Markatos & Kirkcaldy 1983; Markatos 1986; Porterie & Loraud 1994; Nussbaum *et al.* 2006) involve high particle loadings, high pressures (of the order of 1000 atm or more) and high-speed flow. Particle compression and deformation can be significant under these conditions. Nevertheless, interior ballistic models often assume incompressible particles. The intergranular stress for these models lacks the formalism of the kinetic-theory approach. They often describe intergranular stress through empirical correlations that are similar to some frictional–collisional pressure models. As a result, many interior ballistic models can be derived from the more formal kinetic-theory multiphase equations by assuming zero granular temperature (Θ_s) and that the intergranular stress is based solely on a type of frictional–collisional pressure. A multiphase approach similar to interior ballistic models has been used by Rogue *et al.* (1998) to simulate shocks interacting with dense particle curtains.

A limitation of all continuum (or Eulerian) particle models is that they become physically invalid when the number of particles in a computational cell is low and the continuum assumption fails. Under these conditions, the particles act discretely and Lagrangian models, which track individual particles or groups of particles, could be more appropriate. Lagrangian methods can also be used to model the particles in dense granular flow (Helland, Occelli & Tadrist 2000; Nusca, Horst & Newill 2004; Ling *et al.* 2012; Capecelatro & Desjardins 2013). These models can be computationally expensive when there are a large number of particles or groups to track. They are also expensive when particle collision rules have to be applied, as occurs when the granular phase approaches the packing limit.

The approach described in this paper is to couple a continuum kinetic-theory granular model to a compressible gas. The primary focus is on mixtures of granular particles and compressible gas, for which the particle packing can range from very dilute, so that particles do not interact with each other, to densely packed conditions, in which friction and collisions become significant. It is assumed that the particle packing and gas-phase pressure are not so high that elastic waves propagating through the solid material and particle deformation need to be considered.

2.1. Solution difficulties

The underlying difficulties in developing an accurate set of governing equations for coupled gas and granular flow are based on the difficulties of representing important physical interactions, some of which are not defined as clearly as they are for single-phase gaseous flows. This is the topic addressed in the next section (§ 3) on model formulation. Once we have such a model, there remains the issue of how we can use and adapt existing numerical simulation tools to solve specific problems of interest, and what new issues arise from the formulation. In the case of coupled gas–granular flows, the underlying new difficulties are essentially physical, but these also have counterparts in how the solutions must be implemented numerically.

The difficulties in actually solving the equations shown below in § 3 result from a combination of non-conservative interphase coupling terms and numerical stiffness in dilute and dense granular regions. More specifically, we need to deal with: (1) non-conservative ‘nozzling’ terms (Schwendeman, Wahle & Kapila 2006; Karni & Hernández-Dueñas 2010; Crochet & Gonthier 2013) arising from variations of the particle volume fraction within a control volume; (2) a pDV work term that affects the gas as particles enter and leave a control volume (Abgrall & Karni 2010); (3) hyperbolic degeneracy when the intergranular stress in the granular phase is zero; (4) stiffness of the intergranular stress in highly packed regions; and (5) potential loss of hyperbolicity from complex-valued wave speeds.

When the pressure is uniform and the background fluid is stationary (zero velocity), the gas-phase momentum equations with a variation of particle volume fraction reduce to the ‘non-disturbing condition’ (Saurel & Abgrall 1999),

$$\nabla \alpha_g p_g = p_g \nabla \alpha_g. \quad (2.3)$$

Here α_g is the gas-phase volume fraction, p_g is the gas-phase pressure, and the term on the right-hand side is the ‘nozzling term’ due to its analogy with the pDA term in the quasi-one-dimensional gas dynamic nozzle flow equations. Computing the left- and right-hand sides of equation (2.3) independently (Toro 1989; Nussbaum *et al.* 2006) can lead to situations where, for purely numerical reasons, the terms may not balance. This induces unphysical flow and pressure oscillations that can cause numerical solutions to fail (Liou *et al.* 2008).

Another complication is that the compaction wave speed of the particles (analogous to the sound speed of a gas) ranges between zero, when Θ_s is zero or at low particle volume fractions, and approaches infinity at the packing limit. If the compaction wave speed is zero, the result is a pressureless granular gas (sometimes called ‘sticky particle’ models (LeVeque 2004)), which causes numerical problems (specifically, hyperbolic degeneracy (Pelanti & LeVeque 2006)). This means that characteristic-based methods, such as many weighted essentially non-oscillatory (WENO) schemes (Balsara & Shu 2000), or the standard piecewise parabolic method (PPM) (Colella & Woodward 1984) cannot be used to solve these equations in a straightforward manner. Godunov-based methods would require a Riemann solver for the granular phase that is valid in the pressureless state and transitions to a high-pressure state. Despite hyperbolic degeneracy, approximate Riemann solvers were previously designed for pressureless dust (Collins *et al.* 1994; Pelanti & LeVeque 2006), but not for kinetic-theory-based granular models.

The intergranular stress is extremely sensitive to even very small fluctuations of solid volume fraction in dense regions that approach the packing limit. This makes it difficult to develop solution approaches that are both low-dissipation (high-order)

and robust. A difficulty arises because the volume fraction of particles influences the gas and granular phases differently. Particles restrict the area where fluid can flow, and so they accelerate the gas by a nozzling term. On the other hand, the volume fraction controls the compressibility of the granular phase in the same way that density does for the gas phase.

To deal with these numerical problems, the coupled system of equations may be solved using highly dissipative numerical methods. In these cases, refining the grid or using any high-order (therefore more accurate) numerical methods can trigger instabilities that can be masked by excessive numerical diffusion (Nussbaum *et al.* 2006). Recent methods appear to have overcome this for the BN equations (Karni & Hernández-Dueñas 2010; Crochet & Gonthier 2013). Another solution method, used in interior ballistics, is to split the gas and granular conservation equations and solve a Riemann problem for each phase independently and then to compute the non-conservative nozzling and pDV coupling terms separately (Toro 1989), but this approach can violate the non-disturbing condition.

Now high-order, low-dissipation methods for solving the compressible Euler and Navier–Stokes equations are becoming widespread due, in part, to their excellent properties for describing shock waves and compressible turbulence (Grinstein, Margolin & Rider 2007; Thornber *et al.* 2008; Poludnenko & Oran 2010, 2011). The nonlinear filtering effect and added dissipation near sharp gradients that is inherent in shock capturing schemes acts, in many ways, like the explicit filtering and subgrid turbulence models used in traditional large-eddy simulation. In addition, the turbulence in many high-speed shock-laden flows is non-Kolmogorov (Oran & Gamezo 2007), that is, inhomogeneous, non-isotropic and driven by shock–shock interactions and Richtmyer–Meshkov and Rayleigh–Taylor instabilities. Physically accurate subgrid turbulence models usually do not exist for such conditions. Often the only choice in these situations is to use implicit large-eddy simulation, which requires low-dissipation numerical algorithms (Grinstein *et al.* 2007; Thornber *et al.* 2008).

This presents an interesting quandary for multiphase models based on kinetic theory or any other multiphase model where the particles are supposed to be subgrid. In such models, the computational cell size is limited by the particle diameter. It is necessary to have enough particles in a computational cell so that the granular phase can be represented as some kind of fluid. Thus, there are grid limitations on the size of the finest mesh. This limiting computational cell size may be too coarse to capture features of the gas phase, such as the viscous sublayer of a turbulent boundary layer.

In this paper, we first present a model that solves two sets of Euler equations, one for the gas phase and one for the particles, with coupling terms that connect them. We then show how the two sets of equations can be solved using a high-order, low-dissipation numerical method. The technique uses components from existing Riemann solvers and edge interpolation schemes, and incorporates a relatively small modification to the AUSM⁺-up flux (Liou 1996, 2006) for the granular phase. The fluxes and computed states obtained from solving the gas- and granular-phase Riemann problems are assembled to form the convective fluxes and non-conservative terms. Tests of the method that show its ability to preserve the non-disturbing condition, compute multiphase shock-tube problems and simulate strong shocks interacting with dense layers of dust are discussed. Finally, we present comparisons from this model to experimental measurements of shock and particle-curtain interactions (Rogue *et al.* 1998; Ling *et al.* 2012; Wagner *et al.* 2012) and transmitted oblique granular shocks and granular contact surfaces in layers of dust (Fan *et al.* 2007). In future papers, we will discuss extensions that include effects of granular viscosity and heat and mass diffusion, which are not included in this paper.

3. Model formulation

The equations that couple a compressible gas to granular particles are presented. Details, such as proving that the mixture mass, momentum and energy equations are fully conservative, derivation of the entropy equations for each phase, and a hyperbolicity analysis of the model equations, are given in appendix A.

3.1. Euler equations for a single-phase, multispecies flow

The Euler equations for a multicomponent, reacting, compressible gas flow with N_g chemical species can be written as

$$\frac{\partial \rho}{\partial t} + \nabla \cdot (\rho \mathbf{v}) = 0, \quad (3.1)$$

$$\frac{\partial \rho Y_j}{\partial t} + \nabla \cdot (\rho Y_j \mathbf{v}) = \dot{\omega}_j, \quad j = 1, \dots, N_g, \quad (3.2)$$

$$\frac{\partial \rho \mathbf{v}}{\partial t} + \nabla \cdot (\rho \mathbf{v} \mathbf{v}) + \nabla p = \rho \mathbf{g}, \quad (3.3)$$

$$\frac{\partial \rho E}{\partial t} + \nabla \cdot [\mathbf{v}(\rho E + p)] = \rho \mathbf{g} \cdot \mathbf{v}, \quad (3.4)$$

where Y_j , ρ , p , T , E , \mathbf{v} and \mathbf{g} are the mass fraction of species j , density, pressure, temperature, total energy, velocity components and gravitational acceleration vector, respectively. The homogeneous reaction rate due to chemical reactions is denoted by $\dot{\omega}_j$.

The ideal gas equation of state is used to relate the pressure, chemical composition, temperature and density of the gas phase,

$$p = \rho R_u T \sum_{j=1}^{N_g} \frac{Y_j}{M_j}, \quad (3.5)$$

where M_j is the molecular weight of species j and R_u is the universal gas constant. The total energy of the gas phase, E , is given by

$$E = H - \frac{p}{\rho} = \sum_{j=1}^N Y_j \left(h_{fj}^0 + \int_{T_0}^T C_{pj}(s) ds \right) - \frac{p}{\rho} + \frac{\mathbf{v} \cdot \mathbf{v}}{2}, \quad (3.6)$$

where H is the total enthalpy, h_{fj}^0 is the enthalpy of formation at reference temperature T_0 and C_{pj} is the constant-pressure specific heat of species j . Thermodynamic data may be taken from a number of sources. Here data are taken from Goos, Burcat & Rusnic (2010). The sound speed, c , is given by

$$c^2 = \gamma \frac{p}{\rho}, \quad (3.7)$$

where γ is the ratio of specific heats.

3.2. Euler equations for a gas in a multiphase flow

Now we modify (3.1)–(3.4) so they can be used to describe the gas phase in the gas–granular multiphase problem by accounting for the volume taken up by the particles through the gas-phase volume fraction α_g (Ishii & Hibiki 2006),

$$\frac{\partial \alpha_g \rho_g}{\partial t} + \nabla \cdot (\alpha_g \rho_g \mathbf{v}_g) = S^M, \quad (3.8)$$

$$\frac{\partial \alpha_g \rho_g Y_{g,j}}{\partial t} + \nabla \cdot (\alpha_g \rho_g Y_{g,j} \mathbf{v}_g) = \alpha_g \dot{\omega}_{g,j} + S_{g,j}^Y, \quad j = 1, \dots, N_g, \quad (3.9)$$

$$\frac{\partial \alpha_g \rho_g \mathbf{v}_g}{\partial t} + \nabla \cdot (\alpha_g \rho_g \mathbf{v}_g \mathbf{v}_g) + \nabla \alpha_g p_g = p_{int} \nabla \alpha_g + \alpha_g \rho_g \mathbf{g} + \mathbf{S}^p, \quad (3.10)$$

$$\frac{\partial \alpha_g \rho_g E_g}{\partial t} + \nabla \cdot [\alpha_g \mathbf{v}_g (\rho_g E_g + p_g)] = -p_{int} \frac{\partial \alpha_g}{\partial t} + \alpha_g \rho_g \mathbf{g} \cdot \mathbf{v}_g + S_g^E, \quad (3.11)$$

where the subscript g refers to the gas. An important new variable here is α_g , the volume fraction occupied by the gas, so that

$$\alpha_g + \alpha_s = 1 \quad \text{and} \quad \nabla \alpha_g = -\nabla \alpha_s, \quad (3.12a,b)$$

where α_s is the volume fraction of particles. The quantities $Y_{g,j}$, ρ_g , p_g , T_g , E_g and \mathbf{v}_g are the mass fraction of species j , density, pressure, temperature, total energy and velocity vector of the gas, respectively. The pressure at the gas–solid interface around the particles, p_{int} , is used in the nozzling ($p_{int} \nabla \alpha_g$) and pDV work ($-p_{int}(\partial \alpha_g / \partial t)$) terms. The reaction rate due to homogeneous chemical reactions is denoted by $\dot{\omega}_{g,j}$. Additional interphase coupling terms describing transfer of mass, momentum and energy between the gas and the particles are denoted by S^M , $S_{g,j}^Y$, \mathbf{S}^p and S_g^E . These are described in §3.5.

3.3. Euler equations for the particulate phase in a multiphase flow

These equations are similar in form to the Euler equations for the gas phase (Gidaspow 1994). The main difference is that compressibility is introduced by changes in solid volume fraction rather than the material density of the particles, so that compaction waves (analogous to acoustic waves, rarefactions and shocks in a molecular gas) travelling through granular media directly change the particle volume fraction, α_s . The granular-phase governing equations for mass, momentum, pseudo-thermal energy (PTE) and internal energy with N_s species within each particle are

$$\frac{\partial \alpha_s \rho_s}{\partial t} + \nabla \cdot (\alpha_s \rho_s \mathbf{v}_s) = -S^M, \quad (3.13)$$

$$\frac{\partial \alpha_s \rho_s Y_{s,j}}{\partial t} + \nabla \cdot (\alpha_s \rho_s Y_{s,j} \mathbf{v}_s) = \alpha_s \dot{\omega}_{s,j} + S_{s,j}^Y, \quad j = 1, \dots, N_s, \quad (3.14)$$

$$\frac{\partial \alpha_s \rho_s \mathbf{v}_s}{\partial t} + \nabla \cdot (\alpha_s \rho_s \mathbf{v}_s \mathbf{v}_s) + \nabla p_s + \nabla p_{fric} = -\nabla \alpha_s p_g - p_{int} \nabla \alpha_g + \alpha_s \rho_s \mathbf{g} - \mathbf{S}^p, \quad (3.15)$$

$$\frac{\partial \alpha_s \rho_s E_s}{\partial t} + \nabla \cdot (\alpha_s \rho_s E_s \mathbf{v}_s) = -p_s \nabla \cdot \mathbf{v}_s + S_s^{PTE}, \quad (3.16)$$

$$\frac{\partial \alpha_s \rho_s e_s}{\partial t} + \nabla \cdot (\alpha_s \rho_s e_s \mathbf{v}_s) = S_s^E, \quad (3.17)$$

where p_s , p_{fric} , e_s , E_s and $\dot{\gamma}$ are the solids pressure derived from kinetic theory, frictional–collisional pressure, internal energy, PTE and dissipation of E_s due to inelastic particle collisions, respectively. The homogeneous reaction rate of granular species i is denoted by $\dot{\omega}_{s,i}$. The additional interphase coupling terms, $S_{s,j}^Y$, S_s^{PTE} and S_s^E , are discussed in § 3.5.

The PTE, E_s , represents the energy due to random translational motion of the particles,

$$E_s = \frac{3}{2} \Theta_s. \quad (3.18)$$

It is a function of the granular temperature, Θ_s , defined as the mean square of the particle velocity fluctuations. The granular temperature is usually presented in units of $\text{m}^2 \text{s}^{-2}$ rather than K (Gidaspow 1994; Van Wachem *et al.* 2001; Brilliantov & Pöschel 2004).

The ‘normal’ temperature of the particles, T_s , is determined from the solid sensible internal energy, e_s , through

$$e_s = \sum_{j=1}^{N_s} Y_{s,j} \left(e_{fj}^0 + \int_{T_0}^{T_s} C_{V,s,j}(s) ds \right), \quad (3.19)$$

where N_s is the number of species in the solid phase, e_{fj}^0 is an internal energy of formation and $C_{V,s,j}$ is the constant-volume specific heat of species j in the particle phase. This equation assumes that the temperature distribution within each particle is uniform, and so the Biot modulus is small. More complex equations that include the effect of non-uniform temperature distributions inside the particles could be used if the Biot number were large (Koo & Kuo 1977; Markatos & Kirkcaldy 1983; Nussbaum *et al.* 2006). (Note that the granular temperature, Θ_s , is not related to ‘normal’ temperature T_s .)

The density of the solid particles is given by

$$\rho_s = \sum_{j=1}^{N_s} Y_{s,j} \rho_{s,j}(T_s), \quad (3.20)$$

where $\rho_{s,j}$ is the density of species j . In this paper, we take ρ_s to be constant. Relaxing this assumption will be a topic of future work.

The solids pressure, p_s , represents collisional effects of the particles and is given by an equation of state for a granular gas (Gidaspow 1994),

$$p_s = \alpha_s \rho_s \Theta_s [1 + 2(1 + e)\alpha_s g_0], \quad (3.21)$$

where e is the coefficient of restitution. The radial distribution function, g_0 , is defined by (Gidaspow 1994)

$$\frac{1}{g_0} = 1 - \left(\frac{\alpha_s}{\alpha_{s,max}} \right)^{1/3}, \quad (3.22)$$

where $\alpha_{s,max}$ is the packing limit, which is an input parameter commonly set to 0.65 (Agrawal *et al.* 2001; Igci *et al.* 2008), which is representative of the random close-packing limit of uniform spheres (Andreotti *et al.* 2013). Other expressions for g_0 and p_s could be used (see e.g. Kamenetsky *et al.* 2000; Van Wachem *et al.* 2001).

When particles occupy a high volume fraction, frictional–collisional pressure must be added to p_s to describe pressure-like forces that arise as layers of granular material

slide over each other. The inclusion of frictional–collisional pressure has the effect of limiting compaction when Θ_s approaches zero. In highly packed conditions, the binary collision assumption in the Boltzmann equation, which is used to derive the granular-phase equation of state and transport properties, becomes invalid since particles are in contact with several other particles. In these conditions, high rates of inelastic particle collisions can rapidly reduce Θ_s to zero. This results in $p_s = 0$, which allows particles to pack to unphysically high levels. In such dense regions, frictional–collisional pressure is needed to provide the intergranular stress necessary to limit compaction. In this work we use the correlation of Johnson & Jackson (1987),

$$p_{fric} = \begin{cases} 0 & \text{if } \alpha_s < \alpha_{s,crit}, \\ 0.1\alpha_s \frac{(\alpha_s - \alpha_{s,crit})^2}{(\alpha_{s,max} - \alpha_s)^5} & \text{if } \alpha_s \geq \alpha_{s,crit}, \end{cases} \quad (3.23)$$

where $\alpha_{s,crit}$ is 0.5 unless otherwise noted and p_{fric} is in units of Pa. Other expressions for frictional–collisional pressure could be used as well (Koo & Kuo 1977; Markatos & Kirkcaldy 1983; Jenike 1987; Gidaspow 1994; Saurel & Abgrall 1999; Van Wachem *et al.* 2001; Nussbaum *et al.* 2006; Ling *et al.* 2012; Schneiderbauer, Aigner & Pirker 2012). Here the sum of the solids and frictional–collisional pressures is called the total intergranular stress,

$$p_{s,tot} = p_s + p_{fric}, \quad (3.24)$$

to avoid ambiguity with the terminology used for interior ballistics.

(Another approach to limiting compaction of the solid phase is to limit the minimum granular temperature near the packing limit (Kamenetsky *et al.* 2000). This approach, while seemingly *ad hoc*, has a physical basis. The coefficient of restitution, e , is not a constant, as assumed in many kinetic-theory granular multiphase models, but is a function of impact velocity. Higher impact velocities (higher Θ_s) convert more PTE, E_s , into internal energy, e_s , through viscoelastic deformation (Brilliantov & Pöschel 2004). Collisions become increasingly elastic ($e \rightarrow 1$) as the granular temperature decreases. This effect limits both the rate at which Θ_s can decrease and its lower value. Recent granular gas models account for this to some extent (Brilliantov & Pöschel 2004), but, to our knowledge, these have not been used in multiphase flow calculations.)

We do not include the mean kinetic energy in the conservation equation for PTE (equation (3.16)). This avoids small truncation errors of kinetic energy, which can lead to unphysical values of E_s . Dissipation of E_s due to inelastic particle collisions (see § 3.5) often reduces E_s to the point where it is small compared to the mean kinetic energy, $\mathbf{v}_s \cdot \mathbf{v}_s/2$. In a numerical solution of these equations, small errors in the mean kinetic energy can cause small fluctuations of Θ_s , which, in dense-particle regimes, produces severe oscillations of p_s and p_{fric} . Such oscillations can degrade calculations to the point of failure. Decoupling kinetic energy from the PTE equation makes the numerical algorithm more robust. A similar approach is often used in astrophysical calculations (e.g. ASC FLASH Center (2012)). Developing a numerical algorithm that allows us to put the kinetic energy in the PTE equation while maintaining robustness is a topic of ongoing research.

The pressure term in the E_s equation (3.16) does not include flow work from frictional–collisional pressure. This is consistent from a thermodynamics point of view. The p_{fric} models used here are analogous to a barotropic equation of state

for a fluid. It is possible to show, using thermodynamic arguments, that the total energy equation for a barotropic fluid simplifies to the mechanical energy equation (see appendix A). Performing a similar analysis for granular mixtures reveals that only the solids pressure, p_s , contributes to changes in E_s from compression and expansion (changes in volume fraction) of the particles. If the mean kinetic energy were included in the definition of E_s , the friction pressure would enter the total PTE equation (3.18) as $\mathbf{v}_s \cdot \nabla p_{fric}$, while the solids pressure would be present in the usual manner, $\nabla \cdot (\mathbf{v}_s p_s)$ (see (A 9)).

The Euler equations for the granular particles are compressible, similar to those for the gas phase. One key difference, mentioned above, is that this compressibility manifests itself through changes in particle volume fraction in the form of compaction waves. This granular-compaction wave speed can be derived for the particulate phase in the same way that the sound speed can be derived for a real gas (Serna & Marquina 2005). The compaction wave speed for a general granular gas, where friction pressure is only a function of α_s , is

$$c_s^2 = \frac{1}{\rho_s} \left[\frac{\partial p_s^{tot}}{\partial \alpha_s} \bigg|_{\Theta_s} + \frac{2}{3} \frac{\Theta_s \left(\frac{\partial p_s^{tot}}{\partial \Theta_s} \bigg|_{\alpha_s} \right)^2}{\rho_s \alpha_s^2} \right]. \quad (3.25)$$

Then by using the definitions for p_s and p_{fric} (see (3.21) and (3.23)), we find

$$c_s^2 = \Theta_s (A + \frac{2}{3} A^2 + \alpha_s B) + c_{fric}^2, \quad (3.26)$$

where

$$A = 1 + 2(1 + e)\alpha_s g_0, \quad B = 2(1 + e)(g_0 + \alpha_s g'_0), \quad g'_0 = \frac{g_0^2}{3\alpha_{s,max}} \left(\frac{\alpha_{s,max}}{\alpha_s} \right)^{2/3}. \quad (3.27a-c)$$

The frictional contribution to the compaction wave speed (in MKS units) is

$$c_{fric}^2 = \begin{cases} 0 & \text{if } \alpha_s < \alpha_{s,crit}, \\ \frac{1}{\rho_s} \frac{(\alpha_s - \alpha_{s,crit})}{(\alpha_{s,max} - \alpha_s)^5} \left[\alpha_s \left(\frac{1}{5} + \frac{1}{2} \frac{\alpha_s - \alpha_{s,crit}}{\alpha_{s,max} - \alpha_s} \right) + \frac{\alpha_s - \alpha_{s,crit}}{10} \right] & \text{if } \alpha_s \geq \alpha_{s,crit}. \end{cases} \quad (3.28)$$

Several models are available for p_s , p_{fric} and g_0 , as mentioned above (see e.g. Kamenetsky *et al.* 2000; Van Wachem *et al.* 2001; Nussbaum *et al.* 2006). Typically, the coefficient of restitution, e , the random close-packing limit, $\alpha_{s,max}$, and the threshold volume fractions above which p_{fric} becomes non-zero, $\alpha_{s,crit}$, are input parameters. Exploring alternative intergranular stress models and the influence of input parameters is ongoing work.

3.4. The nozzling and pDV work terms

In granular multiphase flows, it is common to choose $p_{int} = p_g$ (Gidaspow 1994). If we further assume that the particle density (ρ_s) is not a function of pressure or intergranular stress, the pDV work term reduces to

$$-p_{int} \frac{\partial \alpha_g}{\partial t} = p_g \frac{\partial \alpha_s}{\partial t} = -p_g \nabla \cdot \alpha_s \mathbf{v}_s - p_g \frac{S^M}{\rho_s}. \quad (3.29)$$

With these expressions, the final momentum equations for the gas and granular phase are

$$\frac{\partial \alpha_g \rho_g \mathbf{v}_g}{\partial t} + \nabla \cdot (\alpha_g \rho_g \mathbf{v}_g \mathbf{v}_g) + \nabla \alpha_g p_g = p_g \nabla \alpha_g + \alpha_g \rho_g \mathbf{g} + \mathbf{S}^p, \quad (3.30)$$

$$\frac{\partial \alpha_s \rho_s \mathbf{v}_s}{\partial t} + \nabla \cdot (\alpha_s \rho_s \mathbf{v}_s \mathbf{v}_s) + \nabla p_s + \nabla p_{fric} = -\alpha_s \nabla p_g + \alpha_s \rho_s \mathbf{g} - \mathbf{S}^p, \quad (3.31)$$

and the gas-phase energy equation becomes

$$\frac{\partial \alpha_g \rho_g E_g}{\partial t} + \nabla \cdot [\alpha_g \mathbf{v}_g (\rho_g E_g + p_g)] = -p_g \nabla \cdot \alpha_s \mathbf{v}_s + \alpha_g \rho_g \mathbf{g} \cdot \mathbf{v}_g + S_g^E, \quad (3.32)$$

where the pDV work associated with phase change is absorbed into S_g^E .

3.5. Interphase coupling terms

Source terms that couple the governing equations for the gas and granular phases (aside from the nozzling and pDV work terms) include drag, convective heat transfer, phase change and dissipation of PTE from inelastic collisions, and lifting forces. We neglect the virtual mass and Basset (history) forces (even though they can be important when computing particle trajectories in some high-speed applications (Ling, Haselbacher & Balachandar 2011a,b)). Selected variable definitions and the source terms and their physical meaning are given in table 1.

The mass exchange term due to phase change is

$$S^M = \dot{M}, \quad (3.33)$$

where the total mass rate of phase change is

$$\dot{M} = \sum_{i=1}^{N_g} S_{g,i}^Y = - \sum_{i=1}^{N_s} S_{s,i}^Y, \quad (3.34)$$

and $S_{g,i}^Y$ and $S_{s,i}^Y$ are the mass rates of production for species i for the gas and granular phases due to phase change. The momentum source terms resulting from phase change, drag and lift are

$$\mathbf{S}^p = \mathbf{f}_{Drag} + \mathbf{f}_{Lift} + \mathbf{v}_{int} \dot{M}. \quad (3.35)$$

The drag force for the particulate mixture is given by the correlation of Gidaspow (1994),

$$\mathbf{f}_{Drag} = K_{sg}(\mathbf{v}_s - \mathbf{v}_g), \quad (3.36)$$

where

$$K_{sg} = \begin{cases} 0.75 C_d \frac{\rho_g \alpha_g \alpha_s |\mathbf{v}_s - \mathbf{v}_g|}{d_s \alpha_s^{2.65}} & \text{if } \alpha_g \geq 0.8, \\ 150 \frac{\alpha_s^2 \mu_g}{\alpha_g d_s^2} + 1.75 \frac{\rho_g \alpha_s |\mathbf{v}_g - \mathbf{v}_s|}{d_s} & \text{if } \alpha_g < 0.8, \end{cases} \quad (3.37)$$

the drag coefficient, C_d , is

$$C_d = \begin{cases} 24(\alpha_g Re)^{-1} [1 + 0.15(\alpha_g Re)^{0.687}] & \text{if } \alpha_g Re < 1000, \\ 0.44 & \text{if } \alpha_g Re \geq 1000, \end{cases} \quad (3.38)$$

α_s, α_g	Volume fraction of the solid (granular) and gas phases, respectively
ρ_s, ρ_g	Material density of the solid and gas phases, respectively
$\mathbf{v}_s, \mathbf{v}_g$	Velocity vector of the solid and gas phases, respectively
p_g	Gas-phase pressure
p_{fric}	Frictional–collisional pressure, (3.23)
p_s	Solids pressure, derived from kinetic theory of granular gases, (3.21)
e_s, e_g	Internal energy of the solid and gas phases, respectively
E_g	Gas-phase total energy
E_s	Pseudo-thermal energy (PTE); energy due to random translational motion of the particles, $E_s = \frac{3}{2} \Theta_s$
Θ_s	Mean square of particle velocity fluctuations
$\dot{\gamma}$	Dissipation of E_s due to inelastic particle collisions, (3.50)
ϕ_{visc}	Sink of PTE due to viscous damping of random translational motion of the particles, (3.47)
ϕ_{slip}	Portion of frictional heating from drag, $(\mathbf{v}_s - \mathbf{v}_g) \cdot \mathbf{f}_{Drag}$, that is diverted into producing E_s , (3.49)
q_{conv}	Convective heat transfer
$\mathbf{f}_{Drag}, \mathbf{f}_{Lift}$	Drag and Magnus lifting forces, (3.36) and (3.40)
\dot{M}	Overall rate of phase change
$E_{g,int}, E_{s,int}, e_{s,int}$	Energy exchange terms during phase change for gas phase, PTE and solid internal energy, (3.51a,b) and (3.52)
\mathbf{v}_{int}	Velocity at the particle–gas interface to define transfer during phase change, (3.41)

TABLE 1. Abbreviated list of variables and their physical interpretation.

and the Reynolds number is defined by

$$Re = \frac{\rho_g |\mathbf{v}_g - \mathbf{v}_s| d_s}{\mu_g}. \quad (3.39)$$

Other forms of the drag coefficient are available in the literature (Syamlal *et al.* 1993; Van Wachem *et al.* 2001; Parmar, Haselbacher & Balachandar 2010), and should be tested, but this is not the subject of this paper

The lift force, \mathbf{f}_{Lift} , is modelled using the Magnus lift force defined by

$$\mathbf{f}_{Lift} = C_l \alpha_s \rho_g (\mathbf{v}_s - \mathbf{v}_g) \times (\nabla \times \mathbf{v}_g), \quad (3.40)$$

where the lift coefficient, C_l , has a value of 0.5 (Drew & Lahey 1987). The influence of the Saffman lift force is currently neglected.

The interfacial velocity used for momentum exchange and energy during phase change are defined using the value from the phase that is losing mass,

$$\mathbf{v}_{int} = \begin{cases} \mathbf{v}_s & \text{if } \dot{M} > 0, \\ \mathbf{v}_g & \text{if } \dot{M} < 0. \end{cases} \quad (3.41)$$

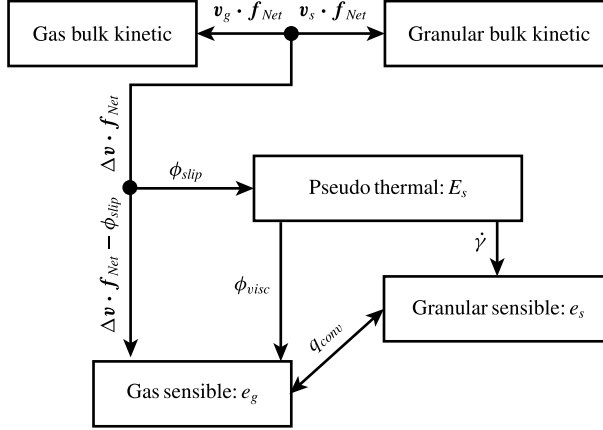


FIGURE 1. Relationship between the energy transfer mechanisms modelled in the source terms to the energy equations, where $f_{Net} = f_{Drag} + f_{Lift}$ and $\Delta v = v_s - v_g$.

The source terms in the energy equations are

$$S_g^E = -q_{conv} + \phi_{visc} - \phi_{slip} + E_{g,int} \dot{M} + (f_{Drag} + f_{Lift}) \cdot v_s, \quad (3.42)$$

$$S_s^E = q_{conv} - e_{s,int} \dot{M} + \dot{\gamma}, \quad (3.43)$$

$$S_s^{PTE} = -\dot{\gamma} - \phi_{visc} + \phi_{slip} - E_{s,int} \dot{M}, \quad (3.44)$$

where $E_{g,int} = H_{g,int} - p_{int}/\rho_s$. These energy exchange terms include, in addition to convective heat transfer, effects from dissipation of PTE from inelastic particle collisions ($\dot{\gamma}$), dissipation of PTE due to viscous effects of particles being immersed in a fluid (ϕ_{visc}), and production of PTE due to drag forces (ϕ_{slip}). The relationship between these energy exchange mechanisms is shown in figure 1.

The convective heat flux between the gas and particles is

$$q_{conv} = 6 \frac{\alpha_s \lambda_g Nu}{d_s^2} (T_g - T_s), \quad (3.45)$$

where the Nusselt number is estimated using the correlation of Gunn (1978),

$$Nu = (7 - 10\alpha_g + 5\alpha_g^2)(1 + 0.7Re^{0.2}Pr_g^{1/3}) + (1.33 - 2.4\alpha_g + 1.2\alpha_g^2)Re^{0.7}Pr_g^{1/3}, \quad (3.46)$$

and Pr_g is the gas-phase Prandtl number.

The model for viscous damping of PTE is adopted from Gidaspow (1994),

$$\phi_{visc} = 3K_{sg}\Theta_s. \quad (3.47)$$

The rate of internal energy production into the gas phase due to frictional heating during particle acceleration is

$$q_{Drag} = \Delta v \cdot f_{Net}, \quad (3.48)$$

where $f_{Net} = f_{Drag} + f_{Lift}$ and $\Delta v = v_s - v_g$. Not all of this internal energy heats the gas as it flows around the particles. Some of this heating is diverted into producing

random translational motion (PTE) of the particles. The production rate of PTE during particle acceleration, ϕ_{slip} , is given by Koch & Sangani (1999) with their correction factor fixed at unity,

$$\phi_{slip} = \frac{81\alpha_s\mu_g^2}{g_0d_s^3\rho_s\sqrt{\pi}} \frac{|\mathbf{v}_g - \mathbf{v}_s|^2}{\sqrt{\Theta_s}}. \quad (3.49)$$

Alternative models for ϕ_{slip} could also be used (e.g. Koch & Sangani 1999), but again these are not the subject of this paper.

The granular dissipation model adopted for this study (Lun *et al.* 1984) is a variant of Haff's cooling law (Haff 1983; Brilliantov & Pöschel 2004),

$$\dot{\gamma} = \frac{12(1 - e^2)g_0\alpha_s^2}{\sqrt{\pi}} \frac{\rho_s\Theta_s^{3/2}}{d_s}. \quad (3.50)$$

Similar to \mathbf{v}_{int} , the interfacial energy exchange terms for phase change are defined by the phase that is losing mass,

$$E_{g,int} = \begin{cases} e_s + E_s + \mathbf{v}_s \cdot \mathbf{v}_s/2 & \text{if } \dot{M} > 0, \\ E_g & \text{if } \dot{M} < 0, \end{cases} \quad E_{s,int} = \begin{cases} E_s & \text{if } \dot{M} > 0, \\ 0 & \text{if } \dot{M} < 0, \end{cases} \quad (3.51a,b)$$

$$e_{s,int} = \begin{cases} e_s & \text{if } \dot{M} > 0, \\ E_g - \mathbf{v}_g \cdot \mathbf{v}_g/2 & \text{if } \dot{M} < 0. \end{cases} \quad (3.52)$$

4. Procedure for solution

The model equations written above comprise sets of coupled inhomogeneous hyperbolic equations, and a number of questions and problems arise when we try to solve these. One type of problem relates to finding appropriate input parameters and models for the different types of particulates, gases and their interactions. Consider dust explosions. The initial conditions, chemical reaction and phase change models, and additional effects, such as particle fragmentation during devolatilization (Dacombe *et al.* 1999), are not always well known. In other situations, such as landing a spacecraft on the granular surface of an asteroid or explosive dispersal of regolith on a comet, even the most basic input parameters such as volume fraction, particle diameter and even the pressure of the background gas are currently unknowable with any degree of certainty.

In addition to the input variables that describe the physical system, there are also a series of interrelated physical and computational issues, which are now discussed. The solution procedure we have adopted is based on a Strang operator splitting scheme, written as

$$\mathbf{U}^{t+2\Delta t} = \mathcal{H}_{xyz}^{\Delta t}(\mathcal{S}^{2\Delta t}(\mathcal{H}_{xyz}^{\Delta t}(\mathbf{U}^t))). \quad (4.1)$$

Here \mathbf{U} is a vector of conserved variables whose solution we seek at time $t + 2\Delta t$, starting with the solution at time t . The operator $\mathcal{H}_{xyz}^{\Delta t}$ represents the integration of the directionally unsplit advection and wave propagation processes for a time step Δt . The operator $\mathcal{S}^{2\Delta t}$ represents integration of the inhomogeneous source terms for a time step of $2\Delta t$. Issues related to the solution for each of these operators will be discussed in turn.

Here the focus is on the hyperbolic terms, which are usually the most challenging numerically. They are a necessary component of any model, regardless of whether granular viscosity is included or hypoplastic granular stress models are applied in solid-like regimes (Z  merli 2013). Chemical reactions and phase changes are discussed elsewhere (Houim & Oran 2015a,b). Details of the numerical solution procedure for both the hyperbolic and source terms can be found in appendix B.

4.1. Solution of the hyperbolic terms

The gas-phase hyperbolic terms, which include gravitational acceleration to ensure hydrostatic equilibrium, are

$$\frac{\partial \alpha_g \rho_g Y_{g,j}}{\partial t} + \nabla \cdot (\alpha_g \rho_g Y_{g,j} \mathbf{v}_g) = 0, \quad (4.2)$$

$$\frac{\partial \alpha_g \rho_g \mathbf{v}_g}{\partial t} + \nabla \cdot (\alpha_g \rho_g \mathbf{v}_g \mathbf{v}_g) + \nabla \alpha_g p_g = p_g \nabla \alpha_g + \mathbf{f}_{Lift} + \alpha_g \rho_g \mathbf{g}, \quad (4.3)$$

$$\frac{\partial \alpha_g \rho_g E_g}{\partial t} + \nabla \cdot (\alpha_g \rho_g \mathbf{v}_g H_g) = -p_g \nabla \cdot \alpha_s \mathbf{v}_s + \mathbf{f}_{Lift} \cdot \mathbf{v}_s + \alpha_g \rho_g \mathbf{g} \cdot \mathbf{v}_g. \quad (4.4)$$

The granular-phase hyperbolic terms are

$$\frac{\partial \alpha_s \rho_s}{\partial t} + \nabla \cdot (\alpha_s \rho_s \mathbf{v}_s) = 0, \quad (4.5)$$

$$\frac{\partial \alpha_s \rho_s Y_{s,j}}{\partial t} + \nabla \cdot (\alpha_s \rho_s Y_{s,j} \mathbf{v}_s) = 0, \quad (4.6)$$

$$\frac{\partial \alpha_s \rho_s \mathbf{v}_s}{\partial t} + \nabla \cdot (\alpha_s \rho_s \mathbf{v}_s \mathbf{v}_s) + \nabla p_s + \nabla p_{fric} = -\alpha_s \nabla p_g - \mathbf{f}_{Lift} + \alpha_s \rho_s \mathbf{g}, \quad (4.7)$$

$$\frac{\partial \alpha_s \rho_s E_s}{\partial t} + \nabla \cdot (\alpha_s \rho_s E_s \mathbf{v}_s) = -p_s \nabla \cdot \mathbf{v}_s, \quad (4.8)$$

$$\frac{\partial \alpha_s \rho_s e_s}{\partial t} + \nabla \cdot (\alpha_s \rho_s e_s \mathbf{v}_s) = 0. \quad (4.9)$$

The semi-discrete form of these equations, implementation details and step-by-step solution procedure are given in appendix B. The lift force is discretized using standard second-order differencing if $\min(\alpha_s) > \alpha_{s,min}$ for all points in the stencil where $\alpha_{min} = 10^{-10}$. A fifth-order numerical method based on Houim & Kuo (2011) is used for spatial discretization. Overcoming the challenges associated with solving the equations with non-conservative terms and the granular fluxes is now discussed.

4.1.1. Non-conservative nozzling and pDV terms

The left-hand side of the governing equation for each phase is in a form that is solvable by many standard numerical algorithms, such as Godunov-style methods, as long as they are solved independently for each phase and also provided that the nozzling term ($p_g \nabla \alpha_g$) in the momentum equation and the pDV work term ($p_g \nabla \cdot \alpha_s \mathbf{v}_s$) for the energy equation are treated as separate source terms. This is a straightforward approach that works well enough if granular interfaces vary smoothly in space, but can fail when there is a steep granular interface (e.g. the edge of a dust layer). The major challenge to obtaining a good numerical solution centres around problems with including the non-conservative nozzling and pDV work terms and enforcing the ‘pressure non-disturbing condition’ (Saurel & Abgrall 1999). This usually cannot be maintained rigorously with a straightforward approach (as discussed in the Introduction) and unphysical pressure oscillations may develop.

An approach that has been shown to work for coupling compressible gases to compressible liquids with sharp material interfaces is the stratified-flow concept developed by Chang & Liou (2007). They consider control volumes for the gas and liquid phases separately. In this approach each computational cell edge is divided into gas–gas, liquid–liquid and gas–liquid sections. The hyperbolic fluxes in each section

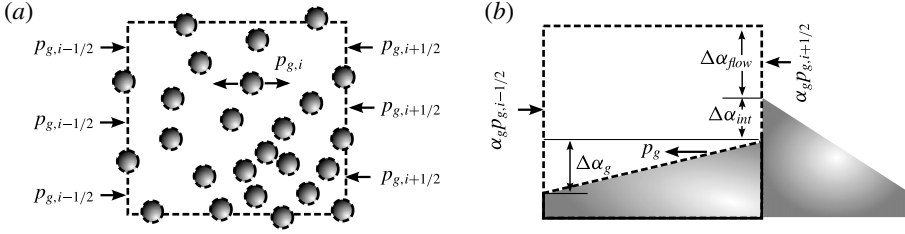


FIGURE 2. Application of the stratified-flow concept to granular multiphase flows in a control volume used to sum the pressure forces. The computational cell index is i and the right and left edges are denoted by $i \pm 1/2$, respectively. (a) Actual control volume. (b) Control volume with particles collapsed.

are computed independently with an appropriate Riemann solver. The flux divergence and pressure gradient terms are assembled from the solution all of these Riemann problems. The application of this concept to granular multiphase flows is illustrated in figure 2.

The stratified-flow concept can be simplified substantially for a granular flow by using the incompressibility assumption of the particles. The volume fraction (while integrating the hyperbolic terms) is controlled by motion of the incompressible particles. This implies that the volume fraction is not a function of the gas-phase state. Thus, the product rule can be applied to the pressure gradient term ($\nabla \alpha_g p_g$), which simplifies the gas-phase momentum equation to

$$\frac{\partial \alpha_g \rho_g \mathbf{v}_g}{\partial t} + \nabla \cdot (\alpha_g \rho_g \mathbf{v}_g \mathbf{v}_g) = -\alpha_g \nabla p_g + \mathbf{f}_{Lift} + \alpha_g \rho_g \mathbf{g}. \quad (4.10)$$

It is straightforward to satisfy the pressure non-disturbing condition with this simplification because there is only one pressure term to compute rather than having to perfectly balance two separate pressure terms.

This simplification used to produce (4.10) is only rigorously possible to make if the particles are assumed to be incompressible. If the particles are compressible, the solid material density would be a function of T_s and the total isotropic stress acting on the particle (i.e. $\rho_s = \rho_s(T_s, p_g, p_{s,tot})$). Conservation of particle mass would then dictate that the solid volume fraction is implicitly a function of ρ_s , since $\alpha_s \rho_s$ is a conserved variable. For example, the high pressure behind a gas-phase shock would increase ρ_s , with a resulting decrease in particle diameter, and, in turn, decrease α_s . Thus, a gas-phase shock would cause a discontinuous decrease of α_s in addition to a pressure jump. As a result, the quantity $\alpha_g p_g$ is, in general, non-differentiable and $\nabla \alpha_g p_g \neq \alpha_g \nabla p_g + p_g \nabla \alpha_g$ across a shock. However, if particle incompressibility is assumed, then $\rho_s = \rho_s(T_s)$ and $\nabla \alpha_g p_g = \alpha_g \nabla p_g + p_g \nabla \alpha_g$, since α_s would then not be an implicit function of the gas-phase pressure and, as a result, would not change discontinuously due to compression behind a gas-phase shock.

One issue that merging the pressure gradient and nozzling terms introduces in (4.10) is that there are no portions of the gas-phase hyperbolic terms that resemble the Euler equations. As a result, standard Godunov methods cannot be used. Despite this, the control volume shown in figure 2 is still valid and the solution to the Riemann problem on the gas-gas fraction of the cell face where gas flows between the particles is physically correct. We use this observation and solve a gas-phase

Riemann problem at the section marked $\Delta\alpha_{flow}$ in figure 2. The pressure computed from this Riemann problem ($p_{g,i+1/2}$) is stored at each cell edge and used to compute the non-conservative pressure term $\alpha_g \nabla p_g$ at each computational cell edge. This is computed in the x -direction by

$$\alpha_g \frac{\partial p_g}{\partial x} \approx \alpha_{g,i} \frac{p_{g,i+1/2} - p_{g,i-1/2}}{\Delta x}, \quad (4.11)$$

where Δx is the width of a computational cell.

The only requirement for evaluating the gas-phase Riemann problem is that pressure is explicitly calculated and is not directly included in the momentum flux. The HLLC (Harten, Lax & van Leer 1983; Toro, Spruce & Speares 1994) and AUSM (Liou 2006) flux schemes can be modified to match this condition. The HLLC flux is used in this work (see appendix B.2). The remaining flux derivatives are computed in a similar manner. For example, the enthalpy flux divergence is

$$\frac{\partial \alpha_g \rho_g u_g H_g}{\partial x} \approx \frac{\alpha_{g,i+1/2} \rho_{g,i+1/2} u_{g,i+1/2} H_{g,i+1/2} - \alpha_{g,i-1/2} \rho_{g,i-1/2} u_{g,i-1/2} H_{g,i-1/2}}{\Delta x}, \quad (4.12)$$

where $\rho_{g,i+1/2}$, $u_{g,i+1/2}$ and $H_{g,i+1/2}$ come from the HLLC Riemann solver and $\alpha_{g,i+1/2}$ is computed using the flux scheme for the granular phase discussed below. More details of the gas-phase solution for the hyperbolic terms can be found in appendix B.

4.1.2. Granular fluxes

Calculation of the granular flux has its own particular set of complications. One issue is its extreme stiffness as the packing limit is approached and the friction pressure and the compaction wave speed increase towards infinity. In such regions, any minute fluctuation of solid volume fraction can produce extremely large changes in friction pressure. The solution we are using to avoid numerical instability is to smoothly degrade the order of the numerical method from fifth-order to first-order as the packing limit is approached. This helps to maintain numerical stability and monotonic solutions of the granular conservative variables. The details of this process are discussed in appendix B.4.

One of the most difficult issues is that the compaction wave speed and solid pressure become zero (1) when the granular temperature is zero or (2) at low volume fractions, resulting in hyperbolic degeneracy (as discussed previously). One approximate Riemann solver used for the particulate phase for a pressureless ($p_{s,tot}=0$) dust model is from Collins *et al.* (1994):

$$F_{s,i+1/2} = \begin{cases} F_s(U_s^L) & \text{if } u_s^L \geq 0 \text{ and } u_s^R > 0, \\ F_s(U_s^R) & \text{if } u_s^L < 0 \text{ and } u_s^R \leq 0, \\ F_s(U_s^L) + F_s(U_s^R) & \text{if } u_s^L > 0 \text{ and } u_s^R < 0, \\ 0 & \text{if } u_s^L < 0 \text{ and } u_s^R > 0, \end{cases} \quad (4.13)$$

where $U_s^{L,R}$ are the left- and right-reconstructed conserved variable vector for the solid phase at edge $i + 1/2$ and F_s is the flux vector of the particle phase, excluding solids pressure and the non-conservative terms. In other locations, where the granular phase is not pressureless, (4.13) is incorrect and a more usual Riemann solver will work. Ideally, however, the same Riemann solver would handle both cases without any *ad hoc* switches, which is the case for the AUSM⁺-up solver (Liou 2006). In

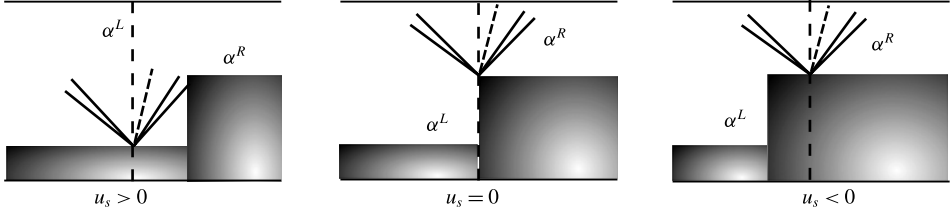


FIGURE 3. Schematic of the gas-phase volume fraction at a cell face at $t=0^+$.

addition to reducing the order of the numerical method to first order in highly packed regions, an additional dissipative term is added to the AUSM flux for the granular phase. Numerical details of the modified AUSM flux for the granular phase are given in § B.4.

AUSM⁺-up is also modified to return $u_{s,i+1/2}$ needed for $p_s \nabla \cdot \mathbf{v}_s$, the quantity $\alpha_{s,i+1/2} u_{s,i+1/2}$ for the pDV work term ($p_g \nabla \cdot \alpha_s \mathbf{v}_s$), and $\alpha_{g,i+1/2}$ needed to complete the gas-phase fluxes. Computation of the gas-phase edge volume fraction is based on where the particles have moved at $t=0^+$, as shown in figure 3, and the gas-phase volume fraction at the cell edge is computed by

$$\alpha_{g,i+1/2} = \begin{cases} \alpha_{g,i+1/2}^L & \text{if } \dot{m}_{s,i+1/2} > 0, \\ \alpha_{g,i+1/2}^R & \text{if } \dot{m}_{s,i+1/2} \leq 0, \end{cases} \quad (4.14)$$

where $\dot{m}_{s,i+1/2}$ is the granular mass flux calculated from the AUSM⁺-up flux (see § B.4 for details). Similarly,

$$\alpha_{s,i+1/2} u_{s,i+1/2} = \begin{cases} \dot{m}_{s,i+1/2} / \rho_{s,i+1/2}^L & \text{if } \dot{m}_{s,i+1/2} > 0, \\ \dot{m}_{s,i+1/2} / \rho_{s,i+1/2}^R & \text{if } \dot{m}_{s,i+1/2} \leq 0, \end{cases} \quad (4.15)$$

$$u_{s,i+1/2} = \begin{cases} \dot{m}_{s,i+1/2} / \alpha_{s,i+1/2}^L \rho_{s,i+1/2}^L & \text{if } \dot{m}_{s,i+1/2} > 0, \\ \dot{m}_{s,i+1/2} / \alpha_{s,i+1/2}^R \rho_{s,i+1/2}^R & \text{if } \dot{m}_{s,i+1/2} \leq 0. \end{cases} \quad (4.16)$$

Then the pressure term in (4.8) is approximated as

$$p_s \frac{\partial u_s}{\partial x} \approx p_{s,i} \frac{u_{s,i+1/2} - u_{s,i-1/2}}{\Delta x}, \quad (4.17)$$

and the pDV term can be approximated as

$$p_g \frac{\partial \alpha_s u_s}{\partial x} \approx p_{g,i} \frac{\alpha_{s,i+1/2} u_{s,i+1/2} - \alpha_{s,i-1/2} u_{s,i-1/2}}{\Delta x}. \quad (4.18)$$

5. Verification test problems

A series of one-dimensional numerical experiments were performed to assess the accuracy and robustness of the method. The solutions were advanced in time using a third-order Runge–Kutta (Spiteri & Ruuth 2003) algorithm with a Courant–Friedrichs–Lewy (CFL) number of 0.5, based on the maximum wave speed, $\lambda_{\max} = \max(|u_g| + c_g, |u_s| + c_s)$. Solid volume fractions below 10^{-10} are set to zero. Boundary conditions

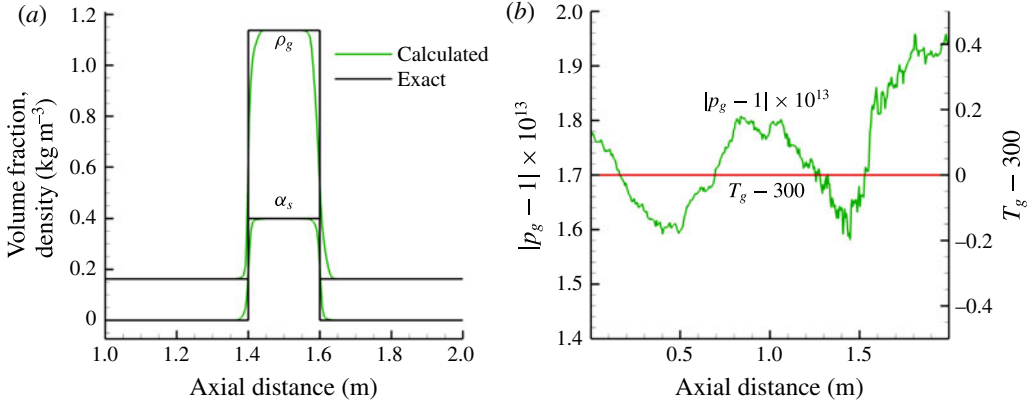


FIGURE 4. (Colour online) Advection of a granular and multicomponent gaseous interface with uniform temperature for a distance of 1 m. (a) Comparison of gas-phase density and α_s to the exact solution and (b) gas-phase temperature and error in pressure.

for the granular phase were either reflected for a symmetry condition or extrapolated for inflow and outflow. The coefficient of restitution for the granular phase is $e = 0.999$ unless specified otherwise. The parameters $\alpha_{s,crit}$ and $\alpha_{s,max}$ were 0.5 and 0.65, respectively. The granular dissipation parameter is $\mathcal{D} = 1$ (see § B.4) unless stated otherwise. Multidimensional tests employ block-structured adaptive mesh refinement (AMR) with the PARAMESH library (MacNeice *et al.* 2000). Refinement is based on smoothness of the mixture density $\rho_m = \alpha_g \rho_g + \alpha_s \rho_g$. Details of how PARAMESH was used for this work can be found in Houim & Kuo (2011). Adaptive mesh refinement was not used for one-dimensional test problems.

5.1. Advection of a particle curtain

Here we examine the ability of the model and numerical algorithm to preserve the pressure non-disturbing condition near a steep granular interface. We advect a curtain of particles with a volume fraction of 40% in a domain with uniform velocity, pressure and temperature of 100 m s⁻¹, 1 atm and 300 K, respectively. To increase the complexity of the calculation, we also place a bubble of pure helium where the particles are located. The gas surrounding the He bubble is pure nitrogen. Specifically, the initial conditions are: $Y_{N_2} = 1$ and $\alpha_s = 0.4$ if $0.4 < x < 0.6$ and $Y_{He} = 1$ and $\alpha_s = 0$ otherwise. The domain was discretized with 200 grid points per metre. Inflow and outflow boundary conditions were used on the left and right boundaries, respectively. We advect the combined granular and gaseous material interface. The particle and helium curtain should be passively advected downstream without changing the pressure and temperature fields. The computed solution, shown in figure 4, indicates that temperature and pressure error are negligible and that the pressure non-disturbing condition is met.

5.2. Two-phase granular shock-tube problem

In this section we test the ability of the model and solution procedure to solve shock-tube problems with low particle volume fraction. The granular-phase solids and frictional-collisional pressures are nearly zero due to the low particle volume

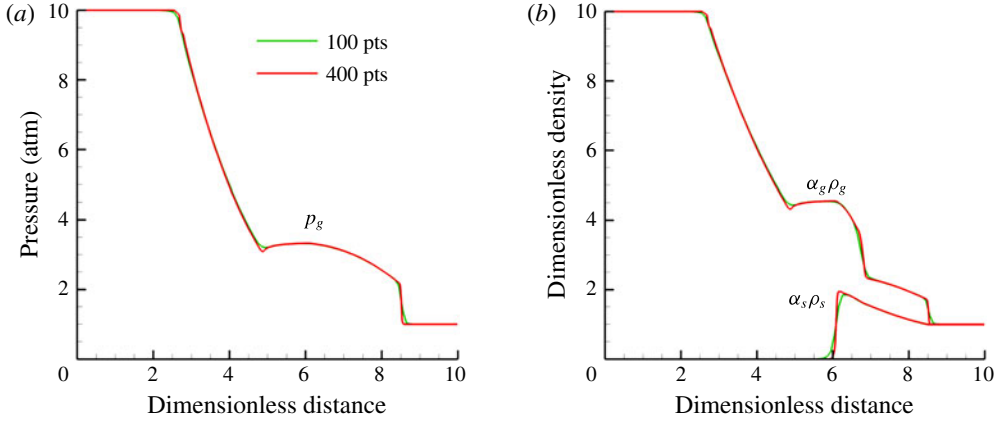


FIGURE 5. (Colour online) Computed (a) gas-phase pressure and (b) bulk densities for the gas and granular phases for the two-phase granular Riemann problem at 184 μs . The densities were scaled by the initial gas-phase density to the right of the interface. The length scale was scaled so that the domain ranges from 0 to 10 to match the output used by Fedorov *et al.* (2007).

fraction. As discussed above, this creates hyperbolically degenerate conditions that are difficult for most standard Riemann solvers to deal with. It is a situation that we must test to ensure that the computed results agree with reference calculations that used specialized Riemann solvers developed for pressureless dust. The initial conditions follow (Saito *et al.* 2003; Fedorov *et al.* 2007):

$$\left. \begin{aligned} p_g^L &= 10 \text{ atm}, & p_g^R &= 1 \text{ atm}, \\ T^L &= 270 \text{ K}, & T^R &= 270 \text{ K}, \\ Y_{g,air}^L &= 1, & Y_{g,air}^R &= 1, \\ \alpha_s^L &= 0, & \alpha_s^R &= 5.172 \times 10^{-4}, \\ \Theta_s^L &= 0, & \Theta_s^R &= 0. \end{aligned} \right\} \quad (5.1)$$

The density, diameter and specific heat of the particles are $\rho_s = 2500 \text{ kg m}^{-3}$, $d_s = 10 \text{ }\mu\text{m}$ and $C_{V,s} = 718 \text{ J kg}^{-1} \text{ K}^{-1}$, respectively. The domain is 0.257798 m in length and the diaphragm is placed at 0.129 m. The solution at 184 μs after the diaphragm is ruptured is shown in figure 5 for two grid spacings. The physics of dust–gas shock-tube problems are well known (Miura & Glass 1982; Saito *et al.* 2003); nevertheless, there are no exact solutions that can be used for verification. Instead, the computed results can be compared with reference solutions from Saito *et al.* (2003) and Fedorov *et al.* (2007). The results, shown in figure 5, compare well with computed results from these references, which indicates that our modified AUSM⁺-up scheme used to compute the granular flux (see § B.4) is accurate when the dust is nearly pressureless.

The burst of the diaphragm sends a shock wave into the low-pressure air and particle mixture, a rarefaction wave into the high-pressure side, and a gas-phase contact surface that passes through the particles. Drag forces between the post-shock gas and particles locally decelerate the gas and produce a subsequent rise in pressure. The pressure increase is due to high-speed gas from regions without particles flowing into and filling a region where gas has been decelerated by drag. The local increase

in pressure produces acoustic waves that propagate towards the rarefaction and cause the hook-like structure at $x \sim 5$. Mechanical and thermal losses of the post-shock gases due to drag also have the effect of weakening the shock, which is illustrated in the next test problem. The two-phase shock wave formed in this test problem corresponds to a Type I structure characterized by Khmel' & Fedorov (2014a,b), where there is a discontinuous gas-phase shock that propagates through the particles with smooth relaxation of granular properties, such as volume fraction, behind the shock.

5.3. Two-phase granular shock-tube problem with a gaseous He–N₂ interface

This problem is similar to the test presented in the previous section, but now we add a gaseous material interface. This examines whether the model and numerical method can produce the correct weak solution for a multiphase shock-tube problem that contains a gaseous material interface with varying γ . Such a situation may exist in a dust explosion when shocks interact with thin dust flames that can separate reactants and products, which have different specific heat ratios. Here the high-pressure side contains pure helium and the low-pressure side contains a mixture of particles and pure N₂. The initial states for this test case are

$$\left. \begin{aligned} p_g^L &= 10 \text{ atm}, & p_g^R &= 1 \text{ atm}, \\ T^L &= 300 \text{ K}, & T^R &= 300 \text{ K}, \\ Y_{g,\text{He}}^L &= 1, & Y_{g,\text{He}}^R &= 0, \\ Y_{g,\text{N}_2}^L &= 0, & Y_{g,\text{N}_2}^R &= 1, \\ \alpha_s^L &= 0, & \alpha_s^R &= 4.555 \times 10^{-4}, \\ \Theta_s^L &= 0, & \Theta_s^R &= 0. \end{aligned} \right\} \quad (5.2)$$

The density, specific heat and restitution coefficient of the particles are 2500 kg m⁻³, 745 J kg⁻¹ K⁻¹ and 0.999, respectively. The domain is 1 m in length and the diaphragm is placed at 0.5 m. The volume fraction of the right state was chosen so that the bulk densities of the gas and granular phases were the same. Calculations were done for two different particle diameters, 10 and 25 μm . The equations were integrated up to 400 μs of physical time and 400 grid points were used in each calculation. A comparison of the computed results to the exact solution for this Riemann problem when particles are not present is shown in § B.2.

The results, shown in figure 6, are qualitatively similar to the previous test problem. The gas-phase pressure in multiphase shock tubes is actually higher if particles are present, even though the shock is weaker (smaller pressure jump and lower speed). Both of these are side effects of mechanical losses to the post-shock gas from drag as discussed earlier. The locally higher value of the solid bulk density and velocity at ~ 0.65 m is caused by a sharp change in the drag force at the He–N₂ contact surface. This causes a pile-up of particles on the nitrogen side of the gas-phase contact surface where the drag force is higher. The solids pressure is very small and has a negligible influence for the low volume fractions in this problem. Spurious oscillations are not present near the granular or He–N₂ contact surfaces, which indicates that the model and solution method can accurately solve two-phase granular shock-tube problems that contain mixtures of gases with varying specific heats.

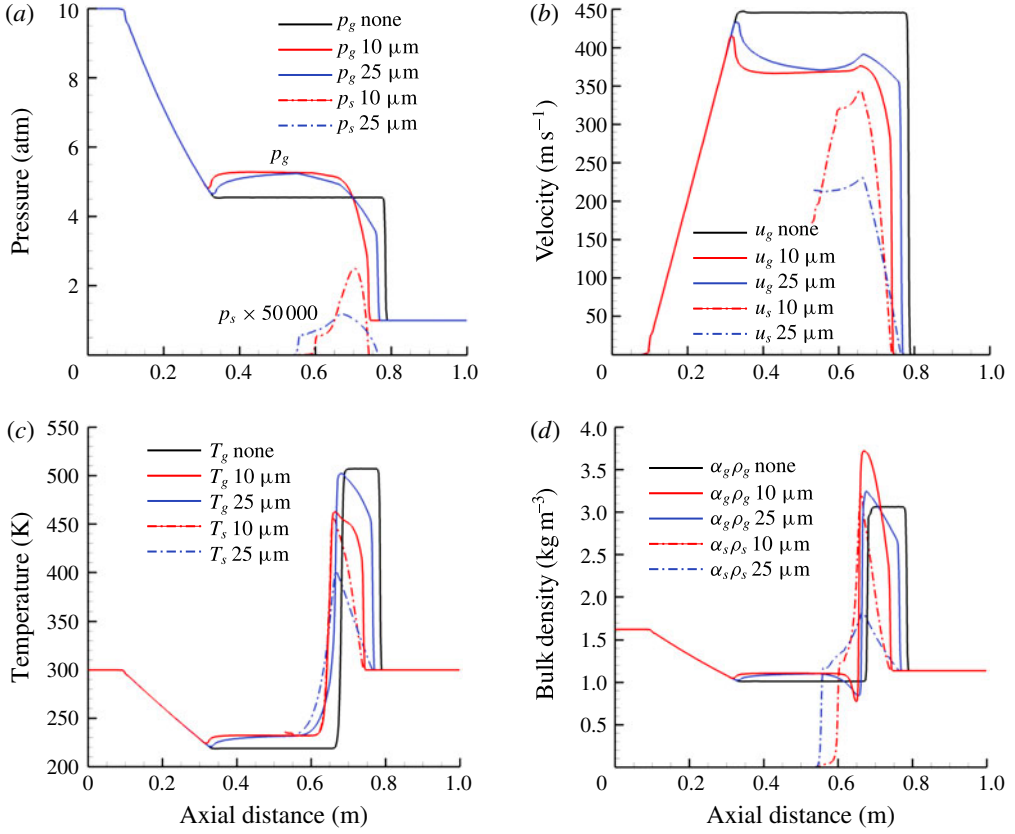


FIGURE 6. (Colour online) Computed (a) gas-phase and solids pressure, (b) velocity, (c) temperature and (d) bulk density for multiphase shock-tube problem with a He-N₂ interface at 400 μs . The solid temperature and velocity are not shown if the particle volume fraction lies below 10^{-8} .

5.4. Dense granular two-phase shock-tube problem

The solids and frictional-collisional pressures were negligible in the previous problems. This test is for a two-phase shock-tube problem with a high driving pressure of 100 atm and a dense particle volume fraction of 40%. This situation tests whether the model can predict relaxation structures of granular shocks (Kamenetsky *et al.* 2000). This case also stresses capabilities of the solution method to compute high-pressure gases interacting with dense granular regions that approach the packing limit with steep granular interfaces. The initial states for this problem are

$$\left. \begin{aligned} p_g^L &= 100 \text{ atm}, & p_g^R &= 1 \text{ atm}, \\ T^L &= 300 \text{ K}, & T^R &= 300 \text{ K}, \\ Y_{g,Air}^L &= 1, & Y_{g,Air}^R &= 1, \\ \alpha_s^L &= 0, & \alpha_s^R &= 0.4, \\ \Theta_s^L &= 0, & \Theta_s^R &= 0. \end{aligned} \right\} \quad (5.3)$$

The domain measures 0.06 m in length and the diaphragm is placed at 0.03 m. The resulting shock structure is advanced for 100 μs on a grid with 1200 computational

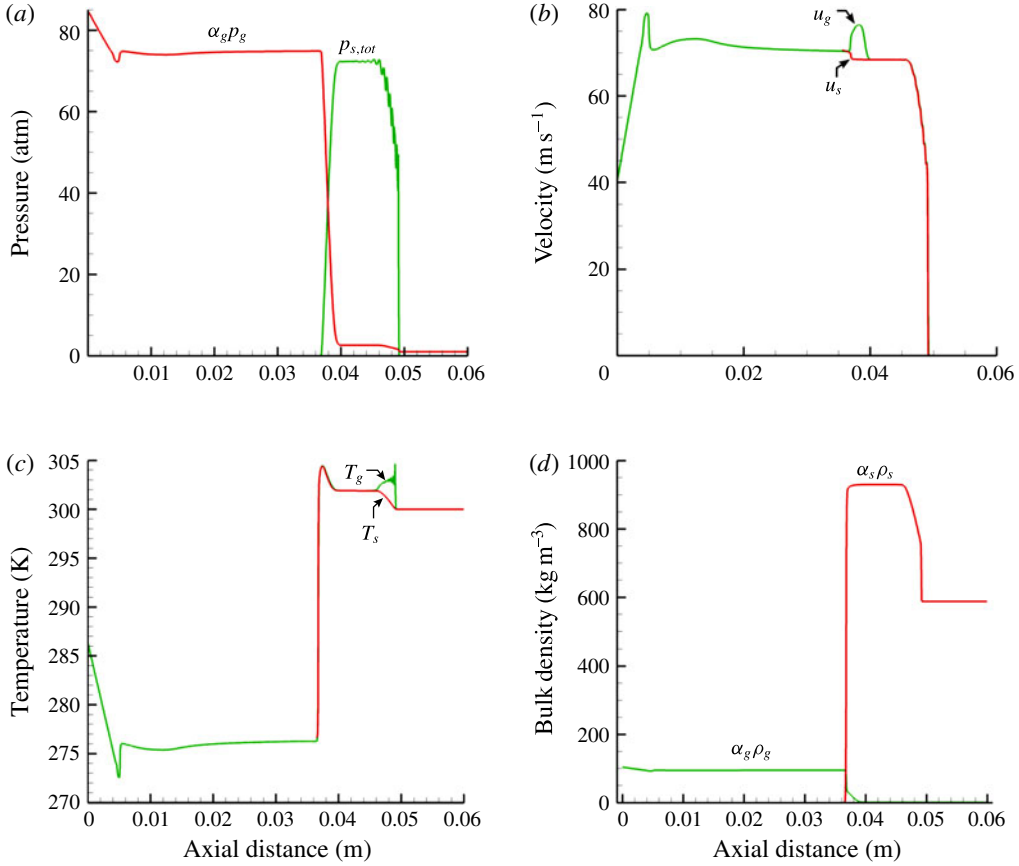


FIGURE 7. (Colour online) Computed (a) pressure, (b) velocity, (c) temperature and (d) bulk density for the dense granular shock-tube problem at $100 \mu\text{s}$ with $e = 0.999$ and $\mathcal{D} = 1$.

cells. The particle diameter, density, specific heat and coefficient of restitution were $5 \mu\text{m}$, 1470 kg m^{-3} , $987 \text{ J kg}^{-1} \text{ K}^{-1}$ and 0.999 , respectively. The volume fraction in this problem approaches the packing limit and additional dissipation was added to the granular phase by setting the hyperbolic dissipation parameter (\mathcal{D}) to 1 (see (B 25) in § B.4). The solution at $100 \mu\text{s}$ is shown in figure 7. The influence of \mathcal{D} and coefficient of restitution (e) on the granular shock structure are shown in figures 8 and 9.

Unlike previous problems shown in §§ 5.1–5.3, particle–particle interactions are now dominant. After the diaphragm is ruptured, a strong granular shock is transmitted into the granular phase due to the combination of Archimedes forces ($\alpha_s \nabla p_g$) and particle drag from the high-pressure gas flowing into the dense layer of particles. Frictional heating from gas initially penetrating the particle bed increases the gas and particle temperature by $\sim 2.5 \text{ K}$ near the contact surface. The computed granular shock has a relaxation structure similar to those reported by Kamenetsky *et al.* (2000). Sources of granular energy, E_s , decrease rapidly away from the granular shock. Without these sources, collisional dissipation of E_s ($\dot{\gamma}$) decreases Θ_s and p_s . Nevertheless, mechanical equilibrium needs to be maintained and the solid volume fraction rises to compensate for the reduction in Θ_s by packing even further to

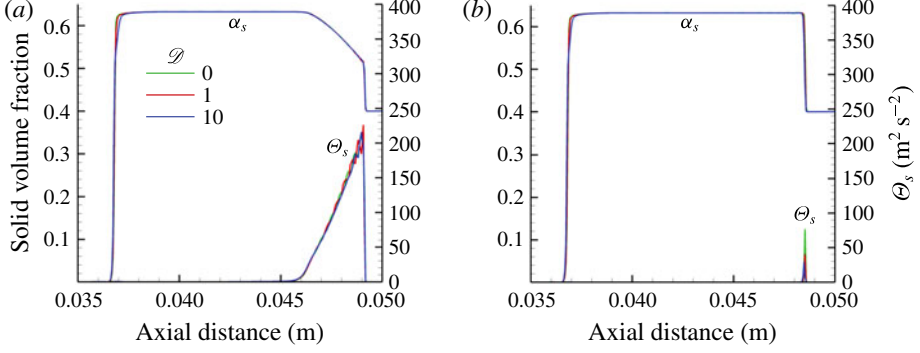


FIGURE 8. (Colour online) Effect of \mathcal{D} and e on calculated profiles of α_s and Θ_s near a granular shock: (a) $e = 0.999$, (b) $e = 0.9$.

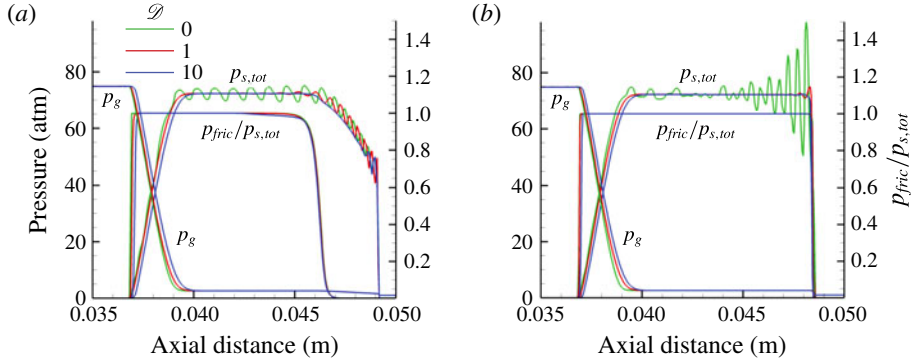


FIGURE 9. (Colour online) Effect of \mathcal{D} and e on calculated profiles of pressure and $p_{fric}/p_{s,tot}$ near a granular shock: (a) $e = 0.999$, (b) $e = 0.9$.

increase the friction pressure. Eventually, the granular temperature decreases to zero, and the total intergranular stress, $p_{s,tot}$, is solely from friction pressure, as shown in figure 9. The granular temperature decreases much faster and the resulting granular shock structure is almost entirely due to friction pressure when the coefficient of restitution is lowered to 0.9.

A weak gas-phase shock-like structure is present at the location of the granular shock. This is due to the increase in particle volume fraction, which compresses the gas and produces a sharp rise in temperature and pressure along with the propagating granular shock. This corresponds to a Type II two-phase granular shock structure characterized by Khmel' & Fedorov (2014a,b), a case where a propagating granular shock drives a weak propagating gas-phase discontinuity along with it. This structure is in contrast to the Type I structure mentioned above, where a gas-phase shock drives a smooth compression of particles (increase of α_s).

A peculiarity of granular systems is that shocks form in granular systems even though c_s and $p_{s,tot}$ can be zero in front of the shock. Assuming that the intergranular stress and particle velocity are zero upstream of the shock and $p_{s,tot} = p_{fric}$, it can be shown through a Rankine–Hugoniot analysis that the shock and post-shock particle

velocities for a purely granular system are

$$u_{shock} = \sqrt{\frac{\alpha_{s,2}}{\alpha_{s,2} - \alpha_{s,1}} \frac{p_{fric}(\alpha_{s,2})}{\alpha_{s,1} \rho_s}}, \quad u_{s,2} = \sqrt{\frac{\alpha_{s,2} - \alpha_{s,1}}{\alpha_{s,2}} \frac{p_{fric}(\alpha_{s,2})}{\alpha_{s,1} \rho_s}}, \quad (5.4a,b)$$

where states 1 and 2 refer to conditions upstream and downstream of the shock, respectively. Applying the post-shock volume fraction shown in figure 8(b) ($\alpha_{s,2} = 0.639$ and $\alpha_{s,1} = 0.4$) produces a shock velocity of 186 m s^{-1} (corresponding to a position of 0.0486 m after $100 \text{ } \mu\text{s}$) and a particle velocity of 69.7 m s^{-1} . These analytical values are close enough to the computed results shown in figures 7(b) and 9(b), considering that the gas phase was not taken into account when computing the analytical post-shock condition.

Small gas-phase temperature oscillations of the order of 1 K are present near the granular shock. These do not cause any numerical instabilities and quickly damp from heat transfer between the gas and granular phases. The bump in gas-phase velocity near the solid contact surface in figure 7 is caused by a reduction in flow area when the gas flows into the particles. Oscillations of pressure, velocity and temperature near the granular interface are not present.

The effectiveness of increasing \mathcal{D} to control oscillations of intergranular stress in dense granular regions is shown in figure 9(b). Severe oscillations of friction pressure are produced when \mathcal{D} is zero, but increasing it to 1 or 10 effectively eliminates the oscillations at the cost of some numerical diffusion of granular interfaces.

5.5. High-pressure outgassing

The previous problem simulated high-pressure gas entering a region of dense particles. The next problem, on the other hand, simulates high-pressure gas leaving a region of dense particles. Consider high-pressure gas that has been injected into a granular layer as a shock passes over. This gas will be ejected when a subsequent expansion wave reduces the pressure at the surface. The outflow induced by the expansion wave will entrain some of the particles. The same initial conditions as the previous problem are used, with the exception that the particles are now located in the high-pressure region of the shock tube,

$$\left. \begin{aligned} p_g^L &= 100 \text{ atm}, & p_g^R &= 1 \text{ atm}, \\ T^L &= 300 \text{ K}, & T^R &= 300 \text{ K}, \\ Y_{g,Air}^L &= 1, & Y_{g,Air}^R &= 1, \\ \alpha_s^L &= 0.4, & \alpha_s^R &= 0.0, \\ \Theta_s^L &= 0, & \Theta_s^R &= 0. \end{aligned} \right\} \quad (5.5)$$

The domain is 0.6 m long and the diaphragm was placed at 0.3 m . The solution at $400 \text{ } \mu\text{s}$ is shown in figure 10 for three grid resolutions.

A right-running shock wave and left-running rarefaction wave are produced, similar to the other shock-tube problems. Now, however, drag and buoyancy forces are induced by the escaping gas from the granular bed, and this ejects particles. This process reduces the particle volume fraction to a profile that is similar in form to the gaseous rarefaction wave. Intense mechanical and thermal losses to the gas phase by entraining particles severely weaken the transmitted gaseous shock. The spikes in temperature near the granular interface are physical and result from particles heating the gas at the gas-phase contact surface and a slight gap between the gas and granular contact surfaces (see figure 10d). If the particles were not present, the temperature would be much higher in the post-shock state and much lower behind the gas-phase contact surface.

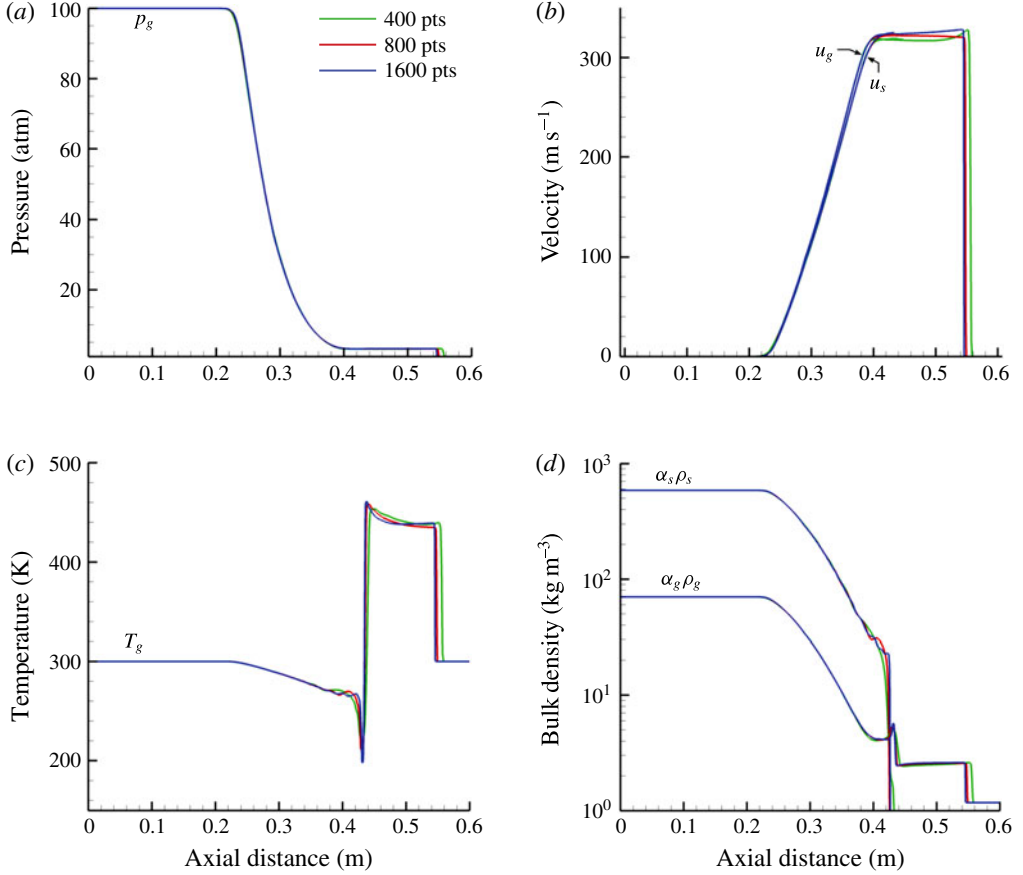


FIGURE 10. (Colour online) Computed (a) gas-phase pressure, (b) velocity, (c) gas-phase temperature and (d) bulk density for high-pressure gaseous ejection from a dense layer of particles at a time of 400 μs . The solid velocity is not shown if the particle volume fraction lies below 10^{-8} .

5.6. Interaction of a shock wave with a low-volume-fraction dust layer

This problem models the interaction of a shock wave with a loose dust layer. A schematic diagram of the geometrical set-up and initial and boundary conditions is shown in figure 11. The heights of the channel and dust layer are 6 cm and 2 cm, respectively. The left edge of the dust pile is placed at 2 cm, and the shock is initially located at 1 cm. A shock of Mach number 1.6 propagates into air at 1 atm and 288 K. The initial volume fraction of the dust layer is 0.04 %. The particle diameter, density and specific heat are $d_s = 5 \mu\text{m}$, $\rho_s = 1470 \text{ kg m}^{-3}$ and $C_{V,s} = 987 \text{ J kg}^{-1} \text{ K}^{-1}$, respectively. Figure 12 shows the computed mixture density at 900 μs for grid spacings of 1.67, 0.83 and 0.42 mm at the finest AMR refinement level. The computed solutions, including the particle and gas-phase vortices, converge with increasing grid resolution.

Figure 12 shows that a vortex is introduced in the gas phase from a shear layer produced as particle drag locally decreases the fluid velocity in the granular layer. The gas-phase vortex entrains some of the particles. The particle vortex does not exactly coincide with the gas-phase vortex due to particle inertia. Mechanical and thermal

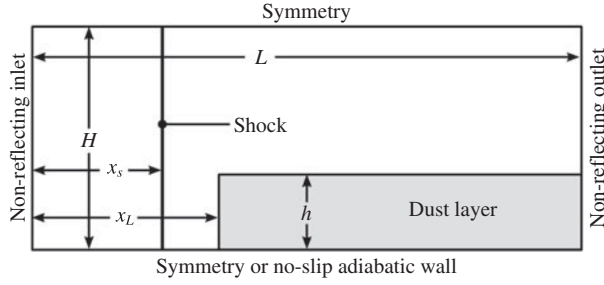


FIGURE 11. Schematic diagram of the initial conditions used for multidimensional test problems.

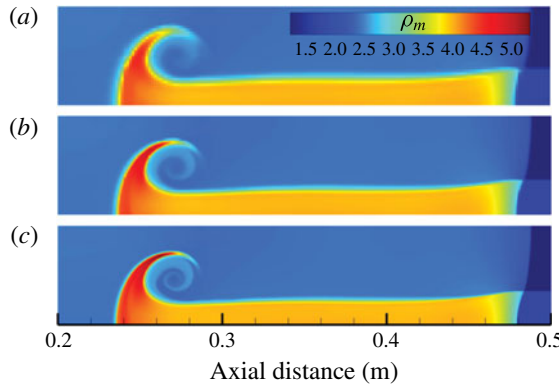


FIGURE 12. (Colour online) Computed mixture density ($\rho_m = \alpha_g \rho_g + \alpha_s \rho_s$, in units of kg m^{-3}) for the low-volume-fraction shock wave and dust layer interaction problem at $900 \mu\text{s}$ for three different grids: (a) $\Delta x_{\min} = 1.67 \text{ mm}$, (b) 0.83 mm and (c) 0.42 mm .

losses from entraining particles cause the shock near the top of the layer to curve and weaken with time. Drag from high-pressure gas entering the layer from the y -direction compresses the particles, which thins the dust layer immediately behind the shock. These results agree well with those of Fedorov & Fedorchenko (2010), in spite of the use of different drag and convective heat transfer models.

6. Experimental validation

The previous tests examined various aspects of the solver and made comparisons to accepted numerical or exact solutions. In this section we compare computed results to experimental measurements. Two geometric configurations are considered. The first configuration is a shock wave interacting with a particle curtain (Rogue *et al.* 1998; Ling *et al.* 2012). Here the position of the particle fronts and shock-wave locations are compared to experimental measurements. The second configuration is a shock wave interacting with a layer of dust, where the transmission angles of an oblique transmitted granular shock and granular contact surface are compared to experimental measurements made by Fan *et al.* (2007). An additional test, not presented in this paper, which uses the same model and solution algorithm, is one in which the high-speed flow behind a shock lifts and entrains dust from a dense layer (Houim & Oran 2015a).

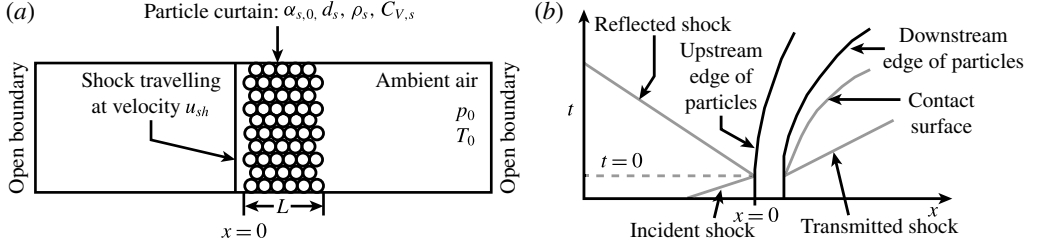


FIGURE 13. Initial conditions and qualitative $x-t$ diagram for the shock wave interacting with a particle curtain.

6.1. Shock and particle-curtain interaction

Here we test the model against nearly one-dimensional multiphase shock-tube experimental measurements in which a shock wave interacts with a curtain of particles. Two conditions are tested: a lower-volume-fraction particle curtain (Wagner *et al.* 2012) and a high-volume-fraction particle curtain (Rogue *et al.* 1998). A schematic diagram of the initial conditions and qualitative $x-t$ diagram of the wave structures produced from a shock interacting with a particle curtain are shown in figure 13. A shock travelling at velocity u_{sh} and strength M_{sh} impacts a curtain of particles of length L and initial volume fraction $\alpha_{s,0}$. Drag forces resulting from gases that enter and flow through the particle bed and buoyancy forces ($\alpha_s \nabla p_g$) from gas pushing on the granular interface accelerate the particles. Gas-phase energy that is not reflected or dissipated to the particles during the acceleration stage is transmitted to the downstream side of the particle bed in the form of a weak shock. The computational domain measured from $-100L$ to $100L$ is discretized with 4000 computational cells. Non-reflecting conditions were used on the left and right boundaries. The upstream edge of the particle curtain is placed at $x=0$.

6.1.1. Particle curtain with $\alpha_{s,0} = 21\%$

Here we compare results of computations to experimental measurements made using the multiphase shock-tube apparatus described in Wagner *et al.* (2012). Specifically, we simulate case 1 of Ling *et al.* (2012), which presents additional data and compares the results of a Lagrangian multiphase model to these measurements. The length of the particle curtain is 2 mm. The initial volume fraction, diameter, density and specific heat of the soda lime particles is 21 %, 115 μm , 2520 kg m^{-3} and 840 $\text{J kg}^{-1} \text{K}^{-1}$, respectively. A Mach 1.66 shock propagates into air initially at 82.7 kPa and 296.4 K. Comparisons of the computed results and experimental data are shown in figure 14.

The locations of the reflected shock, the transmitted shock and the upstream and downstream fronts of the particle curtain are in close agreement with experimental data. The largest discrepancy is the location of the upstream front of particles. The magnitude of this error depends on a precise definition of the particle-curtain edge, which is not stated in Ling *et al.* (2012) or Wagner *et al.* (2012). The computed position of the upstream edge of particles lags experimental results from $x/L = 1.5$ to 2 if a threshold of $\alpha_s = 0.1\%$ or 0.01% is used to define the edge of the particle curtain. On the other hand, the computed position of the upstream particle edge is much closer if a threshold value of $\alpha_s = 1\%$ is used. The computed downstream edge of the particle curtain agrees well with measurements regardless of how the edge of the particle curtain is defined due to the locally high gradient of volume fraction.

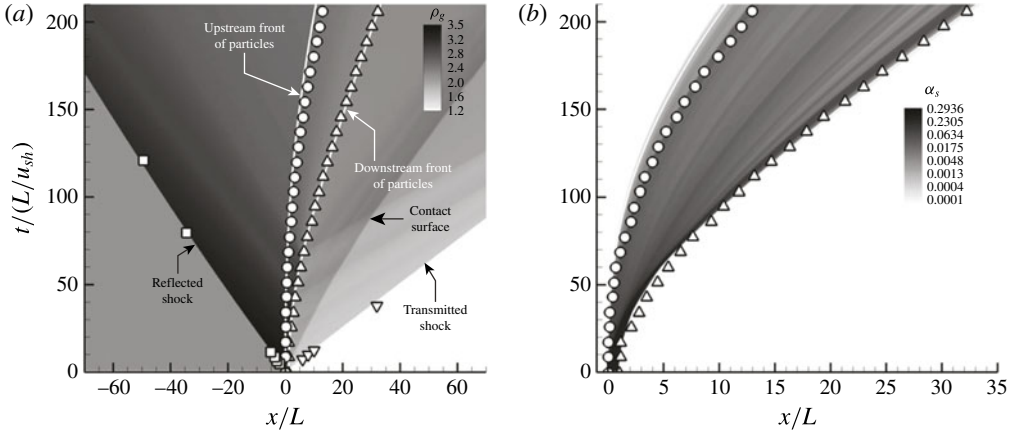


FIGURE 14. Computed x - t diagram of (a) gas-phase density (in units of kg m^{-3}) and (b) solid volume fraction for Mach 1.66 shock interacting with a particle curtain with $L = 2$ mm. The particles were $115 \mu\text{m}$ in diameter and had an initial volume fraction of 21 %. Experimental data presented in Ling *et al.* (2012) and Wagner *et al.* (2012) are represented by symbols.

6.1.2. Particle curtain with $\alpha_{s,0} = 65\%$

The experiment of Rogue *et al.* (1998) has a much larger volume fraction than the previous test ($\alpha_{s,0} = 65\%$). The high initial volume fraction is at a common definition of the random close-packing limit (Agrawal *et al.* 2001; Igci *et al.* 2008). As a result, the parameters $\alpha_{s,crit}$ and $\alpha_{s,max}$ were raised to 65 % and 70 %, respectively, to keep the friction and solids pressures from becoming singular (see (3.21)–(3.23)). The length of the particle curtain is 2 cm. The diameter, density and specific heat of the glass beads that were used to make the curtain are 1.5 mm, 2600 kg m^{-3} and $840 \text{ J kg}^{-1} \text{ K}^{-1}$, respectively. A Mach 1.3 shock propagates into air at 1 atm and 294.2 K. Comparisons of the computed results and experimental data are shown in figure 15.

The results of this test case are qualitatively similar to the previous case. One notable exception is that the transmitted shock is much weaker. This is primarily due to the much higher mechanical and thermal losses created as the shock propagates through the highly packed glass beads. The calculated results match closely with the experimental measurement of the downstream particle front. The upstream front of the particles does not agree as well. This is due, in part, to the ambiguity of defining the edge of particles in the computation, which is undefined in Rogue *et al.* (1998). The upstream front of particles is smoother than the downstream edge, and, as a result, the modelling error is highly sensitive to how the particle edge is defined. If a threshold volume fraction of 1 % is used (see figure 15b), the error is quite large and the front barely appears to move. The agreement between the measurements and the computed results is much better if a threshold volume fraction between 7 % and 10 % is used to define the curtain edge. This ambiguity could be avoided if the particle-curtain edges were precisely defined (based, perhaps, on a threshold volume fraction) in experimental measurements, but this is difficult due to, among other issues, uncertainties of extinction coefficients through particle clouds and details of the experimental apparatus.

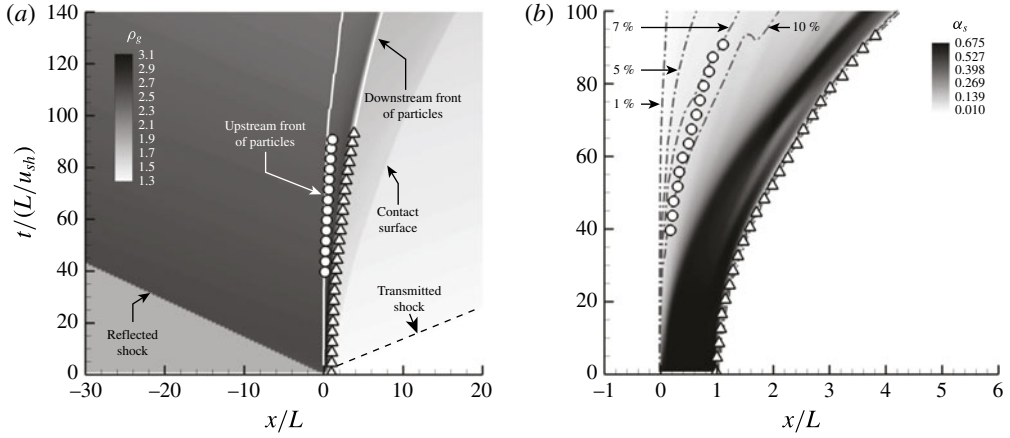


FIGURE 15. Computed x - t diagram of (a) gas-phase density (in units of kg m^{-3}) and (b) solid volume fraction for Mach 1.3 shock interacting with a particle curtain with $L = 2$ cm. The particles were 1.5 mm in diameter and had an initial volume fraction of 65 %. Experimental data of Rogue *et al.* (1998) are represented by symbols.

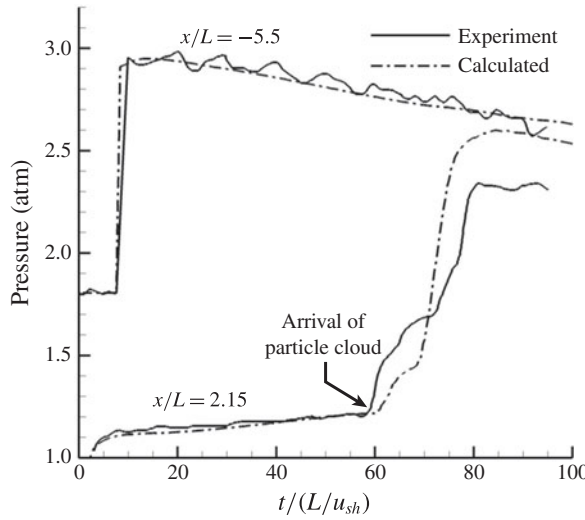


FIGURE 16. Comparison between computed and experimental (Rogue *et al.* 1998) pressure-time traces for a Mach 1.3 shock interacting with a dense particle curtain.

Rogue *et al.* (1998) also measured the pressure-time (p - t) traces at physical distances of -11 cm ($x/L = -5.5$) and 4.3 cm ($x/L = 2.15$) with respect to the upstream edge of the particle curtain. A comparison of the computed to the measured pressure-time traces at these locations is shown in figure 16. The calculations closely match the measurements, and also match the timing and strength of the reflected shock, as well as the subsequent pressure decay as the particle curtain (which acts like a porous moving piston) accelerates. The model results also agree with the strength and timing of the transmitted shock.

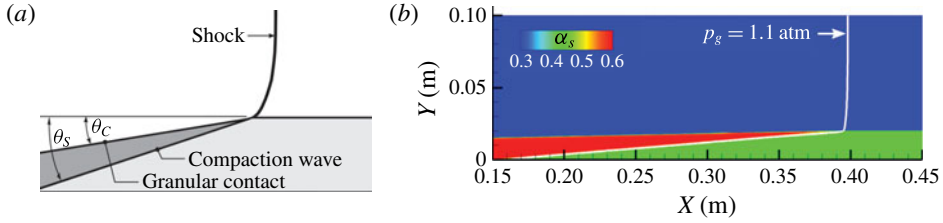


FIGURE 17. (Colour online) Angles of the transmitted compaction wave and granular contact from a shock wave propagating across the dust layer: (a) definition of the angles and (b) computed solution at 100 μs and a grid spacing of 347 μm at the finest level of refinement.

The computed p - t traces do not match as well when the particle cloud arrives at $x/L = 2.15$ and the measured pressure rises rapidly. The sharp pressure rise is produced as the particle bed moves past the measurement location. The p - t trace is essentially a record of the pressure drop as a function of position in the particle curtain as it moves past the measurement location, which is highly sensitive to the volume fraction and drag, and, to some extent, to the models selected for solids and frictional-collisional pressure. (A detailed comparison of the effect of drag and frictional-collisional pressure models on the structure of the particle curtain is beyond the scope of this paper and can be undertaken as a separate study.)

6.2. Transmitted granular oblique shock and contact angles

In the experiment of Fan *et al.* (2007), a shock interacts with a dense layer of dust. The angle that a transmitted compaction wave and granular contact surface make with the horizontal when a shock wave passes over the dust layer, as shown in figure 17(a), was measured. An oblique granular shock is transmitted into the dense layer of dust by forces from high-pressure gas behind the shock pushing on the granular interface as well drag from gases penetrating into the layer. These forces compact the layer and induce an oblique granular contact surface in addition to a transmitted granular shock.

The initial conditions follow the diagram in figure 11. For this test, the layer thickness and domain heights are 2 and 10 cm, respectively. The initial position of the shock is 1 cm, and the left edge of the dust layer is at 0 m. The initial volume fraction was 47%, and the density, diameter, coefficient of restitution and specific heat of the particles were $\rho_s = 1100 \text{ kg m}^{-3}$, $d_s = 15 \text{ }\mu\text{m}$, $e = 0.9$ and $C_{v,s} = 987 \text{ J kg}^{-1} \text{ K}^{-1}$, respectively. The velocity of the shock wave, which propagated into air at 1 atm and 300 K, is 990 m s^{-1} . The bottom boundary was changed to a non-reflecting condition to avoid reflections and increase the measurement distance for the transmitted compaction wave and granular contact angles. The equations were integrated for 100 μs with $\Delta x = 347 \text{ }\mu\text{m}$ at the smallest level of AMR refinement.

The computed solid volume fraction at 100 μs is shown in figure 17(b). The computed transmission angles of the granular contact surface and compaction wave are 1.18° and 4.78° , respectively, which are close to the measured values of 1° – 2° for the contact surface and 4° for the granular shock (Fan *et al.* 2007).

7. Interaction of a shock wave with a dense dust pile

The interaction of a strong Mach 3 shock with a square-edge layer of packed dust is solved to demonstrate the capabilities of the model and solution algorithm. This

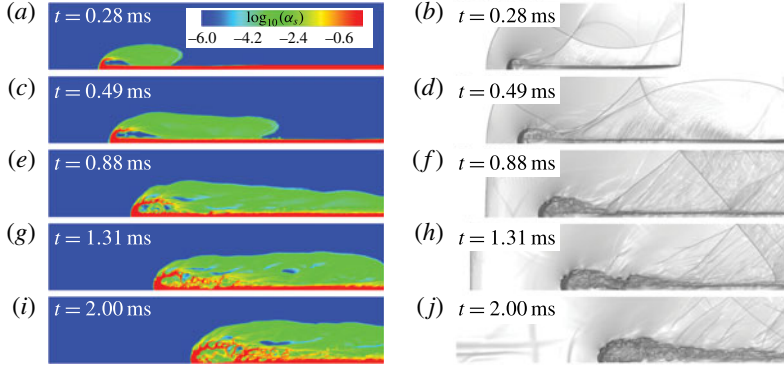


FIGURE 18. (Colour online) Computed time sequence of (a,c,e,g,i) solid volume fraction $\log_{10}(\alpha_s)$ and (b,d,f,h,j) numerical schlieren fields $|\nabla_g|$ for a Mach 3 shock interacting with a dense layer of dust.

problem contains all of the challenging features illustrated with previous test problems, including dense granular regions that approach the packing limit, very dilute granular regions that are hyperbolically degenerate, and sharp granular interfaces that interact with a high-speed flow laden with shocks. The initial and boundary conditions follow figure 11. The height of the domain is 10 cm and the height of the dust layer is 6.67 mm. The left edge of the dust pile is at 20 cm, the shock is initially placed at 19 cm, and the overall domain length is 50 cm. The shock propagates into air at 1 atm and 300 K. The initial volume fraction of the dust is 47 %, which corresponds to typical volume fractions of settled layers of dust (Edwards & Ford 1988; Fan *et al.* 2007). The particle diameter, density and specific heat are $d_s = 5 \mu\text{m}$, $\rho_s = 1470 \text{ kg m}^{-3}$ and $C_{V,s} = 987 \text{ J kg}^{-1} \text{ K}^{-1}$, respectively. The grid spacing at the smallest level of refinement is $\Delta x = 173 \mu\text{m}$.

A sequence showing the solid volume fraction and the numerical gas-phase schlieren ($|\nabla \rho_g|$) is shown in figure 18. The entire domain is shown in each image. Note that there are no pressure oscillations evident in the numerical schlieren in front of the dust layer. Initially, when the shock interacts with the dust layer, intense drag and buoyancy forces act on the particles. This rapidly slows the gas and produces a strong reflected shock that resembles the interaction between a shock and a forward-facing step. The post-shock gases, flowing up and around the front edge of the dust pile, entrain some of the dust and cause it to roll up, similar to earlier results in figure 12. The combination of lift forces and particle–particle interactions strip some of the particles from the surface of the rolled-up layer. This produces a particle cloud with a volume fraction around 0.05 %. Intense shear at the top of the layer and various shock reflections into the dust layer eventually destabilize the boundary layer as the shock moves downstream. This perturbs the top of the dust pile and produces the Mach lines shown in the numerical schlieren at 0.49 ms. Similar Mach lines are shown in experimental shadowgraphs of Fan *et al.* (2007). Perturbing the surface of the layer intensifies turbulence and, as a result, throws more particles up into the post-shock gas. By the end of the calculation, the layer of dust is highly distorted as a result of the turbulence.

Starting at ~ 0.49 ms, lines of locally higher particle volume fraction, called particle streamers, start to form. At 2 ms, the volume fraction in these structures ranges from 0.5 % to 20 %. Such structures have been observed in experiments and computations.

For example, they are seen in incompressible simulations using kinetic-theory-based granular flow models (Agrawal *et al.* 2001; Igci *et al.* 2008), Eulerian–Lagrangian multiphase models that explicitly account for particle collisions (Helland *et al.* 2000), and in riser experiments (Horio & Kuroki 1994). These structures result from two effects: the strong nonlinearity in the drag force as a function of volume fraction, and inelastic collisions locally reducing the solids pressure. Both of these effects produce dense clumps of particles that tend to move as a group and can be around 10 particle diameters in width (Agrawal *et al.* 2001).

8. Summary and conclusions

In this paper, we have presented a granular multiphase model suitable for high-speed flows that can be laden with shocks and contain particle concentrations ranging from dilute to nearly packed. The model resembles some of the granular multiphase models used for incompressible flows (Syamlal *et al.* 1993; Gidaspow 1994), but here it is extended to fully compressible flows. Two sets of Euler equations are coupled, one for the gas phase and another for the granular phase. Intergranular stress representing collisional and friction effects is described through the solids and frictional–collisional pressures. The phases can be coupled by drag, convective heat transfer, phase change, etc. Nevertheless, many physical assumptions, discussed in §§ 3 and 4, were made to justify this form when the flow speed is high and it is compressible. Extending the model to include the granular viscosity terms in the gas- and liquid-like regimes is a topic of ongoing work.

The largest limitation to the model is that it is not valid in the solid-like regions of granular flow, which could be important for simulating phenomena with deep piles of granular material such as dunes. Another limitation is the inability to predict accurately the behaviour of cohesive granular materials, such as powders made of very small particles or wet sand. Overcoming these limitations would necessitate adding granular viscous stresses that resemble plastic flow (Jop, Forterre & Pouliquen 2006; Zèmerli 2013), stress relaxation models (Zhang 2005), or even Hooke’s law (Andreotti *et al.* 2013). Development of stress models for the solid-like regime for pure granular materials (no interstitial fluid between the grains) is an active research area.

There is great uncertainty in the drag and convective heat transfer correlations in high-speed and densely packed regions. We found that the drag correlation of Gidaspow (1994) works surprisingly well, given that it was developed for low-speed flows. Arguably, drag models for compressible flow (Parmar *et al.* 2010) would be better in low-volume-fraction regions, but have not been extended to dense regions. The Ergun equation (the limit of (3.37) at high particle volume fraction) is probably more appropriate in dense regions that resemble a fluidized bed, but has not been extended to compressible flows. Similar problems exist with convective heat transfer and other correlations needed for interphase coupling.

In addition to developing the physical model, a numerical solution algorithm was designed to solve the coupled gaseous and granular Euler equations. The main challenge was to overcome difficulties associated with the non-conservative nozzling and pDV work terms that couple the gas and granular phases. The nozzling term was simplified using the assumption of particle incompressibility, which means that the material density of the particles is not a function of pressure or intergranular stress. This allows the pressure gradient and nozzling terms to be combined in the gas-phase momentum equation, which ruins the usual conservative form needed

to apply most numerical methods for computational gas dynamics. We overcame this issue by observing that the gas-phase Riemann problem is still physically valid in the region between particles where gas can flow. The solution of these Riemann problems provides the gas-phase parameters needed to approximate the flux divergence and non-conservative terms. The granular fluxes were computed using an AUSM scheme that was modified to increase dissipation in highly packed regions, where the intergranular stress becomes mathematically stiff, and to compute accurate fluxes when the intergranular stress is zero.

The numerical tests indicate that the model and numerical solution procedure can compute a wide range of two-phase granular flow scenarios, including two-phase shock tubes, granular shocks and shocks interacting with dust layers. The model was experimentally verified against measurements of shocks interacting with particle curtains and transmitted oblique granular shocks. The model results match closely with experimental measurements in almost all of the cases. One notable exception is the location of the upstream edge of the particle curtain in the Rogue *et al.* (1998) test. Here the success of the model is highly dependent on the precise definition of the particle-curtain edge. With one definition, the model agreement is good; while, with other definitions, the model agreement is poor. It would greatly aid further improvement of granular multiphase models if definitions of parameters, such as the particle-curtain edge, were explicitly provided in publications presenting the experimental results. Nevertheless, this can be quite complex, since it is highly dependent on many details, such as imaging technique, wavelength of the light source, spectral response of the camera, and uncertainties in computing extinction coefficients of particle curtains.

The model and numerical solution method presented in this paper are currently being used to simulate complex phenomena related to layered coal-dust explosions (Houim & Oran 2015a,b). It is also applicable to other problems, such as dust lifting behind a shock wave or behaviour of regolith under impact.

Acknowledgements

This work was supported by the National Research Council Postdoctoral Research Associateship Program and the University of Maryland through Minta Martin Endowment Funds in the Department of Aerospace Engineering, and through the Glenn L. Martin Institute Chaired Professorship at the A. James Clark School of Engineering. We would like to thank all of the reviewers for providing valuable comments and suggestions that improved the quality of this paper. We would also like to thank S. Lai and O. Ugarte for helping with the revised manuscript.

Appendix A. Analysis of the governing equations

In this section, the mass, momentum and energy equations are derived for the mixture, and the entropy equation is derived for each phase. Lastly, the bounds of hyperbolicity (i.e. the parameter space where the wave speeds are all real-valued) for the model are analysed. First, an internal energy to the granular phase due to frictional–collisional pressure (E_{fric}) needs to be derived.

A.1. Derivation of E_{fric} and the total pseudo-thermal energy equation

Consider the change of internal energy for a real gas,

$$de = C_v dT + \left[T \frac{\partial p}{\partial T} \Big|_v - p \right] dv, \quad (\text{A } 1)$$

where v is the specific volume. The analogous change in energy for a granular material can be computed using a similar equation, but replacing T with Θ_s and v with $(\alpha_s \rho_s)^{-1}$ (Gidaspow 1994). Assuming ρ_s is not a function of intergranular stress, we have

$$dE_s^{tot} = \frac{3}{2} d\Theta_s - \frac{1}{\rho_s \alpha_s^2} \left[\Theta_s \frac{\partial p_{s,tot}}{\partial \Theta_s} \Big|_{\alpha_s} - p_{s,tot} \right] d\alpha_s, \quad (\text{A } 2)$$

where $E_s^{tot} = E_s + E_{fric}$. Substituting (3.21), (3.23) and (3.24) into (A 2) gives

$$dE_s^{tot} = dE_s + dE_{fric} = \frac{3}{2} d\Theta_s + \frac{p_{fric}}{\rho_s \alpha_s^2} d\alpha_s. \quad (\text{A } 3)$$

Recall that $E_s = \frac{3}{2} \Theta_s$, then $dE_s = \frac{3}{2} d\Theta_s$. Removing the PTE from (A 3) leaves a frictional–collisional internal energy,

$$dE_{fric} = \frac{p_{fric}}{\rho_s \alpha_s^2} d\alpha_s, \quad (\text{A } 4)$$

which, upon integration, gives

$$E_{fric}(\alpha_s) = \int_0^{\alpha_s} \frac{p_{fric}}{\rho_s \alpha^2} d\alpha. \quad (\text{A } 5)$$

Using the fact that p_{fric} and E_{fric} are functions of α_s only (see (3.23)), it can be shown that

$$\frac{\partial \alpha_s \rho_s E_{fric}}{\partial t} + \nabla \cdot [\alpha_s \rho_s \mathbf{v}_s E_{fric}] + \nabla \cdot \mathbf{v}_s p_{fric} = \mathbf{v}_s \cdot \nabla p_{fric}, \quad (\text{A } 6)$$

or

$$\frac{\partial \alpha_s \rho_s E_{fric}}{\partial t} + \nabla \cdot [\alpha_s \rho_s \mathbf{v}_s E_{fric}] + p_{fric} \nabla \cdot \mathbf{v}_s = 0. \quad (\text{A } 7)$$

Thus, the net contribution of p_{fric} to the total granular energy equation is purely mechanical.

Recognizing that the total stress acting on the particles is given by $p_{s,tot} + \alpha_s p_g$, the total energy equation for the granular phase is

$$\begin{aligned} & \frac{\partial \alpha_s \rho_s (E_s^{tot} + E_s^{KE})}{\partial t} + \nabla \cdot [\mathbf{v}_s (\alpha_s \rho_s (E_s^{tot} + E_s^{KE}) + p_{s,tot} + \alpha_s p_g)] \\ & = p_g \nabla \cdot \alpha_s \mathbf{v}_s + \alpha_s \rho_s \mathbf{v}_s \cdot \mathbf{g} - \mathbf{v}_s \cdot \mathbf{S}^p + S_s^{PTE}, \end{aligned} \quad (\text{A } 8)$$

where E_s^{KE} is the kinetic energy of the granular phase and $p_g \nabla \cdot \alpha_s \mathbf{v}_s$ is the pDV work done by the particulate phase ($-p_g \partial \alpha_s / \partial t$) due to changing particle volume.

Using (A 6), equation (A 8) becomes

$$\begin{aligned} & \frac{\partial \alpha_s \rho_s (E_s + E_s^{KE})}{\partial t} + \nabla \cdot \{ \mathbf{v}_s [\alpha_s \rho_s (E_s + E_s^{KE}) + p_s + \alpha_s p_g] \} + \mathbf{v}_s \cdot \nabla p_{fric} \\ & = p_g \nabla \cdot \alpha_s \mathbf{v}_s + \alpha_s \rho_s \mathbf{v}_s \cdot \mathbf{g} - \mathbf{v}_s \cdot \mathbf{S}^p + S_s^{PTE}, \end{aligned} \quad (\text{A } 9)$$

which is the form of (3.16) that would be solved if mechanical energy was included. Removing the mechanical energy equation,

$$\frac{\partial \alpha_s \rho_s E_s^{KE}}{\partial t} + \nabla \cdot (\alpha_s \rho_s \mathbf{v}_s E_s^{KE}) + \mathbf{v}_s \cdot \nabla (p_s + p_{fric}) = -\alpha_s \mathbf{v}_s \cdot \nabla p_g + \alpha_s \rho_s \mathbf{v}_s \cdot \mathbf{g} - \mathbf{v}_s \cdot \mathbf{S}^p, \quad (\text{A } 10)$$

from (A 9) produces equation (3.16):

$$\frac{\partial \alpha_s \rho_s E_s}{\partial t} + \nabla \cdot (\alpha_s \rho_s E_s \mathbf{v}_s) = -p_s \nabla \cdot \mathbf{v}_s + S_s^{PTE}. \quad (3.16)$$

A.2. Governing equations for the mixture

Summing the continuity equations (3.8) and (3.13), the momentum equations (3.30) and (3.31), and the energy equations (3.32), (A 8) and (3.17) produces the mixture equations:

$$\frac{\partial \alpha_s \rho_s + \alpha_g \rho_g}{\partial t} + \nabla \cdot [\alpha_s \rho_s \mathbf{v}_s + \alpha_g \rho_g \mathbf{v}_g] = 0, \quad (\text{A } 11)$$

$$\frac{\partial \alpha_s \rho_s \mathbf{v}_s + \alpha_g \rho_g \mathbf{v}_g}{\partial t} + \nabla \cdot [\alpha_s \rho_s \mathbf{v}_s \mathbf{v}_s + \alpha_g \rho_g \mathbf{v}_g \mathbf{v}_g] + \nabla [p_g + p_s^{tot}] = [\alpha_s \rho_s + \alpha_g \rho_g] \mathbf{g}, \quad (\text{A } 12)$$

$$\begin{aligned} & \frac{\partial \alpha_s \rho_s \mathbf{v}_s E_s^{total} + \alpha_g \rho_g E_g}{\partial t} + \nabla \cdot [\alpha_s \rho_s \mathbf{v}_s E_s^{total} + \alpha_g \rho_g \mathbf{v}_g E_g] \\ & + \nabla \cdot [\mathbf{v}_s (\alpha_s p_g + p_s^{tot}) + \alpha_g \mathbf{v}_g p_g] = (\alpha_s \rho_s \mathbf{v}_s + \alpha_g \rho_g \mathbf{v}_g) \cdot \mathbf{g}, \end{aligned} \quad (\text{A } 13)$$

where $E_s^{total} = E_s^{tot} + E_s^{KE} + e_s$. The mixture governing equations satisfy the mathematical requirements of a conservation law (Toro 1999), provided that E_{fric} is added to the total energy (even though its net contribution is purely mechanical) and gravitational acceleration is neglected.

A.3. Entropy equations for each phase

The entropy equation for each phase will be computed. For simplicity, all inhomogeneous source terms and the lifting force are ignored. Chemical potential is also neglected because phase change and chemical reaction are not considered as part of this analysis.

A.3.1. Gas-phase entropy

In terms of the substantial derivative ($D(\dots)/Dt = \partial(\dots)/\partial t + \mathbf{v} \cdot \nabla(\dots)$), the $T ds$ relation is

$$T_g \frac{Ds_g}{Dt} = \frac{De_g}{Dt} - \frac{p_g}{\rho_g^2} \frac{D\rho_g}{Dt}, \quad (\text{A } 14)$$

where s_g and e_g are the entropy and internal energy of the gas phase, respectively. The gas-phase internal energy equation, in non-conservative form, is

$$\frac{De_g}{Dt} = -\frac{p_g}{\alpha_g \rho_g} \nabla \cdot [\alpha_s \mathbf{v}_s + \alpha_g \mathbf{v}_g]. \quad (\text{A } 15)$$

Using the gas and granular continuity equations produces

$$\frac{D\rho_g}{Dt} = -\frac{\rho_g}{\alpha_g} \nabla \cdot [\alpha_s \mathbf{v}_s + \alpha_g \mathbf{v}_g]. \quad (\text{A } 16)$$

Substituting De_g/Dt and $D\rho_g/Dt$ into the Tds relation gives

$$\frac{Ds_g}{Dt} = 0. \quad (\text{A } 17)$$

A.3.2. Granular-phase entropy

The granular phase contains two energy equations. The thermal energy (e_s) is a function of T_s , but we could also choose $e_s = e_s(s_s^T)$, where s_s^T is an entropy associated with e_s . In non-conservative form, the granular thermal energy equation is

$$\frac{De_s}{Dt} = 0, \quad (\text{A } 18)$$

which implies that

$$\frac{Ds_s^T}{Dt} = 0. \quad (\text{A } 19)$$

The analogous Tds relation for the fluctuating and frictional–collisional granular energy is (Gidaspow 1994)

$$\theta_s \frac{Ds_s^{tot}}{Dt} = \frac{D}{Dt}[E_s + E_{fric}] - \frac{p_s + p_{fric}}{\rho_s \alpha_s^2} \frac{D\alpha_s}{Dt}, \quad (\text{A } 20)$$

where s_s^{tot} is the entropy associated with E_s and E_{fric} . If E_{fric} is put into (3.16) and the resulting expression is cast in non-conservative form, we get

$$\frac{D}{Dt}[E_s + E_{fric}] = - \frac{(p_s + p_{fric})}{\alpha_s \rho_s} \nabla \cdot \mathbf{v}_s. \quad (\text{A } 21)$$

Then substituting the above expression and the Lagrangian derivative of solid volume fraction,

$$\frac{D\alpha_s}{Dt} = -\rho_s \nabla \cdot \mathbf{v}_s, \quad (\text{A } 22)$$

into the $\Theta_s ds$ equation gives

$$\frac{Ds_s^{tot}}{Dt} = 0. \quad (\text{A } 23)$$

A.4. Mixture entropy

Notice that the $\Theta_s ds_s$ relation (A 20) produces an entropy. Nevertheless, s_s^{tot} has different units (s_s^{tot} is unitless) than the entropy for a gas or liquid (s_s^T and s_g have units of $\text{J kg}^{-1} \text{K}^{-1}$). As a result, it is difficult to define a mixture entropy equation if the net production of any form of entropy is non-zero,

$$(\alpha_s \rho_s + \alpha_g \rho_g) s_{mix} \neq \alpha_g \rho_g s_g + \alpha_s \rho_s (s_s^T + s_s^{tot}), \quad (\text{A } 24)$$

because the units do not even match! Instead, the mixture entropy would have to be defined by something like

$$(\alpha_s \rho_s + \alpha_g \rho_g) s_{mix} = \alpha_g \rho_g s_g + \alpha_s \rho_s (s_s^T + C s_s^{tot}), \quad (\text{A } 25)$$

where C is a constant needed to match units and give a proper scaling of s_s^{tot} with respect to s_s^T . Determining the value of C for this system is a rather deep scientific question and would be a research topic in itself.

A.5. Hyperbolicity of the governing equations

It is well known that the governing equations for compressible multiphase mixtures have regions where hyperbolicity may be lost due to complex-valued wave speeds for the fully coupled system (Nussbaum *et al.* 2006; Lhuillier *et al.* 2013). Fixing this issue has been an ongoing endeavour for dispersed multiphase flows for decades. Models that exhibit conditional hyperbolicity need to be properly verified and validated to ensure realistic results.

First, the governing equations (in one dimension) are transformed into a primitive variable formulation,

$$\frac{\partial \mathbf{P}}{\partial t} + \mathbf{A}(\mathbf{P}) \frac{\partial \mathbf{P}}{\partial x} = 0, \quad (\text{A } 26)$$

where $\mathbf{A}(\mathbf{P})$ is a coefficient matrix and the vector of primitive variables is chosen as $\mathbf{P} = (\rho_g, u_g, s_g, \alpha_s, u_s, s_s^{tot}, e_s)^T$. Realizing that pressure and intergranular stress can be written in terms of their respective entropies ($p_g = p_g(\rho_g, s_g)$ and $p_{s,tot} = p_{s,tot}(\alpha_s, s_s^{tot})$), we have

$$\frac{\partial p_g}{\partial x} = c_g^2 \frac{\partial \rho_g}{\partial x} + \left. \frac{\partial p_g}{\partial s_g} \right|_{\rho_g} \frac{\partial s_g}{\partial x}, \quad (\text{A } 27)$$

$$\frac{\partial p_s}{\partial x} = \rho_s c_s^2 \frac{\partial \alpha_s}{\partial x} + \left. \frac{\partial p_s^{tot}}{\partial s_s^{tot}} \right|_{\alpha_s} \frac{\partial s_s^{tot}}{\partial x}. \quad (\text{A } 28)$$

Using the previous two equations and the earlier results that $Ds_g/Dt = 0$ and $Ds_s^{tot}/Dt = 0$, the coefficient matrix is

$$\mathbf{A}(\mathbf{P}) = \begin{bmatrix} u_g & \rho_g & 0 & \rho_g \frac{u_s - u_g}{\alpha_g} & \rho_g \frac{\alpha_s}{\alpha_g} & 0 & 0 \\ \frac{c_g^2}{\rho_g} & u_g & \frac{1}{\rho_g} \left. \frac{\partial p_g}{\partial s_g} \right|_{\rho_g} & 0 & 0 & 0 & 0 \\ 0 & 0 & u_g & 0 & 0 & 0 & 0 \\ 0 & 0 & 0 & u_s & \alpha_s & 0 & 0 \\ \frac{c_g^2}{\rho_s} & 0 & \frac{1}{\rho_s} \left. \frac{\partial p_g}{\partial s_g} \right|_{\rho_g} & \frac{c_s^2}{\alpha_s} & u_s & \frac{1}{\alpha_s \rho_s} \left. \frac{\partial p_s^{tot}}{\partial s_s^{tot}} \right|_{\alpha_s} & 0 \\ 0 & 0 & 0 & 0 & 0 & u_s & 0 \\ 0 & 0 & 0 & 0 & 0 & 0 & u_s \end{bmatrix}. \quad (\text{A } 29)$$

The wave speeds of the coupled system are the eigenvalues of $\mathbf{A}(\mathbf{P})$. The characteristic polynomial for $\mathbf{A}(\mathbf{P})$ is

$$(u_g - \lambda)(u_s - \lambda)^2 \left\{ [c_g^2 - (u_g - \lambda)^2][c_s^2 - (u_s - \lambda)^2] - c_g^2 \frac{\alpha_s}{\alpha_g} \frac{\rho_g}{\rho_s} (u_g - \lambda)^2 \right\}. \quad (\text{A } 30)$$

Three of the seven wave speeds are immediate and given by $\lambda = u_g, u_s, u_s$. A clean analytic solution is not possible for the remaining four wave speeds. Instead, the range of parameters that produce complex-valued wave speeds is examined. First, the characteristic polynomial for the remaining wave speeds is non-dimensionalized to

$$(1 - \chi^2)[C_r^2 - (M_{slip} - \chi)^2] - z\chi^2 = 0, \quad (\text{A } 31)$$

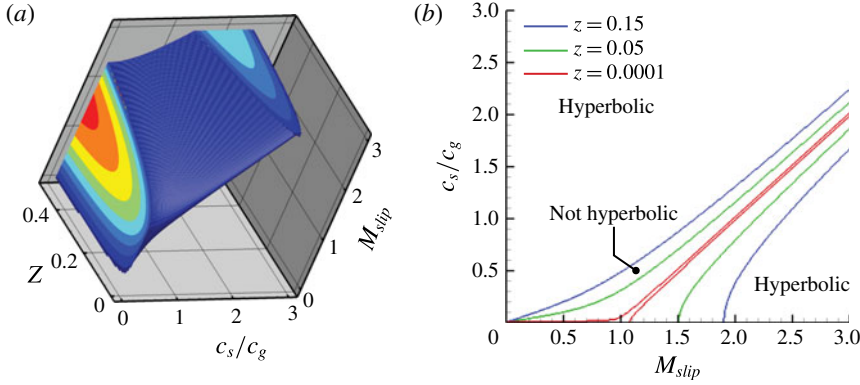


FIGURE 19. (Colour online) Contour plots indicating regions where hyperbolicity is lost due to complex-valued wave speeds. (a) Largest imaginary component of the wave speed and the isosurface that bounds the region where hyperbolicity is lost. (b) Slices along values of z that are representative of the numerical experiments presented in this paper.

where $\chi = (\lambda - u_g)/c_g$, $M_{slip} = (u_s - u_g)/c_g$, $C_r = c_s/c_g$ and $z = \alpha_s \rho_g / \alpha_g \rho_s$. The range of dimensionless parameters that produce complex-valued wave speeds is shown in figure 19

The parameter z is typically small for gas-particle mixtures and ranges from 2×10^{-7} for the test shown in figure 5 to approximately 0.15 for the test shown in figures 7–9. The experimental test case shown in figure 14 has $z = 0.0001$ (based on the initial conditions). With the exception of hyperbolic degeneracy when $c_s/c_g \approx 0$, the numerical experiments usually do not have situations where hyperbolicity is lost.

Consider the case shown in figure 19(b), with $z = 0.15$, which corresponds to the test shown in figures 7–9. Owing to the high volume fraction, frictional-collisional pressure dominates, $c_s/c_g \approx 4.3$ and the slip Mach number is, at most, of the order of 0.06. Examining figure 19(b) reveals that this test case is safely in a hyperbolic region. Therefore, the oscillations in figures 7–9 cannot be caused by loss of hyperbolicity.

The numerical experiment shown in figure 14 has a value $z = 0.0001$, but $c_s \approx 0$ due to the maximum solid volume fraction of approximately 35%. This case loses hyperbolicity in a manner similar to the degenerate situation encountered in the dilute limit, which did not present instabilities in figures 5, 6 and 14.

Practical situations for gas-particle mixtures probably do not exist in the diagonal band where the equations lose hyperbolicity. Even if a solution momentarily existed in this band, drag would quickly relax the velocity between the gas and solid phases, which would reduce M_{slip} and, in most cases, move the solution trajectory into a hyperbolic region. The numerical solution approach presented in this paper seems to suppress any major numerical instabilities even if hyperbolicity is momentarily lost.

A fully hyperbolic model can be obtained with wave speeds $\lambda = u_g$, u_s , u_s , $u_g \pm c_g$, $u_s \pm c_s$ if the nozzling, pDV and Archimedes force ($\nabla \alpha_s p_g$ for the particle momentum equation) terms are neglected and the gas-phase pressure gradient term is written as ∇p_g rather than $\nabla \alpha_g p_g$. Removing all of these terms is physically difficult to justify (Lhuillier *et al.* 2013), and, based on our numerical experiments, does not reduce the pressure oscillations in figure 9; nor did it alleviate the instabilities that forced the removal of the kinetic energy from (3.16). Therefore, the challenges we overcame in developing the numerical method to solve the model equations were probably not due to a loss of hyperbolicity.

Appendix B. Details of the numerical implementation

B.1. Semi-discrete forms of the hyperbolic terms

The semi-discrete forms of (4.2)–(4.9) in one dimension for a computational cell with index i with grid size Δx and computational cell edges located at $i \pm 1/2$ are

$$\frac{d(\alpha_g \rho_g Y_{g,j})_i}{dt} = - \frac{\alpha_{g,i+1/2} \rho_{g,i+1/2}^- u_{g,i+1/2}^- Y_{g,j,i+1/2}^- - \alpha_{g,i-1/2} \rho_{g,i-1/2}^+ u_{g,i-1/2}^+ Y_{g,j,i-1/2}^+}{\Delta x}, \quad (\text{B } 1)$$

$$\begin{aligned} \frac{d(\alpha_g \rho_g u_g)_i}{dt} = & - \frac{\alpha_{g,i+1/2} \rho_{g,i+1/2}^- u_{g,i+1/2}^- u_{g,i+1/2}^- - \alpha_{g,i-1/2} \rho_{g,i-1/2}^+ u_{g,i-1/2}^+ u_{g,i-1/2}^+}{\Delta x} \\ & - \alpha_{g,i} \frac{p_{g,i+1/2}^- - p_{g,i-1/2}^+}{\Delta x} + \alpha_{g,i} \rho_{g,i} g_x, \end{aligned} \quad (\text{B } 2)$$

$$\begin{aligned} \frac{d(\alpha_g \rho_g E_g)_i}{dt} = & - \frac{\alpha_{g,i+1/2} \rho_{g,i+1/2}^- u_{g,i+1/2}^- H_{g,i+1/2}^- - \alpha_{g,i-1/2} \rho_{g,i-1/2}^+ u_{g,i-1/2}^+ H_{g,i-1/2}^+}{\Delta x} \\ & - p_{g,i} \frac{\alpha_{s,i+1/2} u_{s,i+1/2} - \alpha_{s,i-1/2} u_{s,i-1/2}}{\Delta x} + \alpha_{g,i} \rho_{g,i} u_{g,i} g_x, \end{aligned} \quad (\text{B } 3)$$

$$\frac{d(\alpha_s \rho_s)_i}{dt} = - \frac{\dot{m}_{s,i+1/2} - \dot{m}_{s,i-1/2}}{\Delta x}, \quad (\text{B } 4)$$

$$\frac{d(\alpha_s \rho_s Y_{s,j})_i}{dt} = - \frac{\dot{m}_{s,i+1/2} Y_{s,j,i+1/2} - \dot{m}_{s,i-1/2} Y_{s,j,i-1/2}}{\Delta x}, \quad (\text{B } 5)$$

$$\begin{aligned} \frac{d(\alpha_s \rho_s u_s)_i}{dt} = & - \frac{\dot{m}_{s,i+1/2} u_{s,i+1/2} + p_{s,tot,i+1/2} - \dot{m}_{s,i-1/2} u_{s,i-1/2} - p_{s,tot,i-1/2}}{\Delta x} \\ & - \alpha_{s,i} \frac{p_{g,i+1/2}^- - p_{g,i-1/2}^+}{\Delta x} + \alpha_{s,i} \rho_{s,i} g_x, \end{aligned} \quad (\text{B } 6)$$

$$\frac{d(\alpha_s \rho_s E_s)_i}{dt} = - \frac{\dot{m}_{s,i+1/2} E_{s,i+1/2} - \dot{m}_{s,i-1/2} E_{s,i-1/2}}{\Delta x} - p_{s,i} \frac{u_{s,i+1/2} - u_{s,i-1/2}}{\Delta x}, \quad (\text{B } 7)$$

$$\frac{d(\alpha_s \rho_s e_s)_i}{dt} = - \frac{\dot{m}_{s,i+1/2} e_{s,i+1/2} - \dot{m}_{s,i-1/2} e_{s,i-1/2}}{\Delta x}. \quad (\text{B } 8)$$

Here subscript j is the species index, u_s and u_g are the x -component of the gas- and granular-phase velocity vector, $\dot{m}_s = \alpha_s \rho_s u_s$ is the mass flux for the solid phase, and g_x is the x -component of the gravitational acceleration vector. Gas-phase variables with $+$ and $-$ superscripts (e.g. $\rho_{g,i+1/2}^+$ and $\rho_{g,i-1/2}^-$) are needed for the double-flux model (Billet & Abgrall 2003) discussed below. Examination of the semi-discrete equations shows that the gas and granular phases are coupled directly through the volume fraction, gas-phase pressure gradient, and pDV work from particles entering and leaving the control volume. The edge-centred fluxes, pressure, velocities, volume fraction, etc. needed to assemble the conservative and non-conservative convective terms are calculated with approximate solutions to separate gas and granular Riemann problems discussed below.

B.2. HLLC flux for the gas phase

HLLC has been modified to return a vector of the solution state of the Riemann problem $\mathbf{R}_g = (\rho_g, Y_{g,j}, u_g, p_g, E_g)^T$ rather than the fluxes. This allows the pressure

to be separated from the momentum flux, so that the term $\alpha_g \nabla p_g$ can be directly approximated with (4.11). The approximate solution to the Riemann problem at computational cell edge $i + 1/2$ is given by

$$\mathbf{R}_{g,i+1/2} = \begin{cases} \mathbf{R}_{g,i+1/2}^L & \text{if } 0 \leq S^L, \\ \mathbf{R}_g^{L*} & \text{if } S^L \leq 0 \leq S^*, \\ \mathbf{R}_g^{R*} & \text{if } S^* \leq 0 \leq S^R, \\ \mathbf{R}_{g,i+1/2}^R & \text{if } S^R \leq 0, \end{cases} \quad (\text{B } 9)$$

where

$$\mathbf{R}_g^K = \begin{bmatrix} \rho_g^K \\ Y_{g,j}^K \\ u_g^K \\ p_g^K \\ E_g^K \end{bmatrix}, \quad \mathbf{R}_g^{K*} = \begin{bmatrix} \rho_g^{K*} \\ Y_{g,j}^{K*} \\ S^* \\ p^* \\ E_g^{K*} \end{bmatrix}, \quad (\text{B } 10a,b)$$

and the superscript K refers to either L or R , which are the left- or right-reconstructed states at edge $i + 1/2$. The density and total energy in the middle states are

$$\rho_g^{K*} = \rho_g^K \frac{S^K - u_g^K}{S^K - S^*}, \quad E_g^{K*} = E_g^K + \frac{p^* S^* - p_g^K u_g^K}{\rho_g^K (S^K - u_g^K)}, \quad (\text{B } 11a,b)$$

where ρ_g^K is computed from the interpolated pressure, temperature, species mass fractions and the equation of state. The velocity of the gas-phase contact surface (S^*) is

$$S^* = \frac{p_g^R - p_g^L + \rho_g^L u_g^L (S^L - u_g^L) - \rho_g^R u_g^R (S^R - u_g^R)}{\rho_g^L (S^L - u_g^L) - \rho_g^R (S^R - u_g^R)} \quad (\text{B } 12)$$

and the pressure at the contact surface (p^*) is

$$p^* = p_g^L + \rho_g^L (S^L - u_g^L) (S^* - u_g^L). \quad (\text{B } 13)$$

The left and right wave speeds are estimated using a Roe-averaged approach (Einfeldt *et al.* 1991)

$$S^L = \min(u_g^L - c_g^L, \tilde{u}_g - \tilde{c}_g), \quad S^R = \max(u_g^R + c_g^R, \tilde{u}_g + \tilde{c}_g), \quad (\text{B } 14)$$

where

$$\left. \begin{aligned} \tilde{\mathbf{v}}_g &= \frac{\sqrt{\rho_g^L} \mathbf{v}_g^L + \sqrt{\rho_g^R} \mathbf{v}_g^R}{\sqrt{\rho_g^L} + \sqrt{\rho_g^R}}, \quad \tilde{H}_g = \frac{\sqrt{\rho_g^L} H_g^L + \sqrt{\rho_g^R} H_g^R}{\sqrt{\rho_g^L} + \sqrt{\rho_g^R}}, \\ \tilde{c}_g &= [(\gamma - 1)(\tilde{H}_g - \frac{1}{2} \tilde{\mathbf{v}}_g \cdot \tilde{\mathbf{v}}_g)]^{1/2}, \end{aligned} \right\} \quad (\text{B } 15)$$

with

$$H_g^K = \frac{\gamma}{\gamma - 1} \frac{p_g^K}{\rho_g^K} + \frac{1}{2} \mathbf{v}_g^K \cdot \mathbf{v}_g^K. \quad (\text{B } 16)$$

The primitive variable vectors $\mathbf{R}_{g,i+1/2}^L$ and $\mathbf{R}_{g,i+1/2}^R$ needed for HLLC are interpolated using a fifth-order accurate method (Houim & Kuo 2011). The interpolation method

uses fifth-order symmetric bandwidth-optimized WENO (Martín *et al.* 2006) with nonlinear error controls (Taylor, Wu & Martín 2007) and an adaptive total variation diminishing (TVD) slope limiter to interpolate primitive variables to the cell edges. The low-Mach-number velocity adjustment procedure of Thornber, Mosedale & Drikakis (2007) is used to reduce numerical dissipation for the gas phase. We rotate the HLLC Riemann solver (Houim & Kuo 2011; Huang *et al.* 2011) near shocks to avoid carbuncle-related anomalies (Pandolfi & D'Ambrosio 2001).

B.3. Treatment of variable specific-heat ratios

The ratio of specific heats is, in general, a function of temperature and chemical composition. Advecting a multicomponent gaseous interface can produce severe pressure oscillations that may eventually cause the method to go unstable in extreme cases. The quasi-conservative double-flux model (Billet & Abgrall 2003) prevents these oscillations and has been shown to work well for a variety of complex reacting flows such as premixed flames, cellular structure of detonations and shock waves interacting with diffusion flames (Houim & Kuo 2011).

At the start of the calculation, the specific heats for each gaseous species are stored in linear interpolation tables with uniform temperature increments of $\Delta T = 1$ K. If $T_m < T_g < T_{m+1}$, the constant-pressure specific heat of species j is

$$C_{pj}(T_g) = a_j^m T_g + b_j^m, \quad (\text{B } 17)$$

where m is the temperature interval at which T_g resides in the table, and a_j^m and b_j^m are tabulated slope and offset parameters. The specific total energy of the mixture is then calculated in a form similar to a constant-property single-component ideal gas,

$$E_g = h_0^m + \frac{p_g}{\rho_g(\gamma - 1)} + \frac{\mathbf{v}_g \cdot \mathbf{v}_g}{2}, \quad (\text{B } 18)$$

where

$$\left. \begin{aligned} h_0^m &= \sum_{j=1}^{N_g} Y_{g,j} (\bar{h}_{j0}^m - \bar{b}_j^m T_m), \quad \bar{h}_{j0}^m = h_{fi}^0 + \sum_{k=1}^m \left[\int_{T_{k-1}}^{T_k} (a_j^k s + b_j^k) ds \right], \\ \bar{b}_j^m &= \frac{a_j^m}{2} (T_g + T_m) + b_j^m. \end{aligned} \right\} \quad (\text{B } 19)$$

An extension of the analysis performed by Billet & Abgrall (2003) to multiphase mixtures shows that, if $u_g = u_s = u$ and $\nabla p_g = \nabla u = 0$, the uniform pressure and velocity in a multicomponent granular flow are preserved if γ and $\alpha_g \rho_g h_0^m$ are frozen in each cell for the entire time step. Thus, the gas mixture in each computational cell is treated as its own constant-property single-component ideal gas. The flux at each cell face must be calculated twice as a consequence: once for the cell on the left side of the face using γ_i and $\alpha_{g,i} \rho_{g,i} h_{0,i}^m$, and then again for the cell on the right using γ_{i+1} and $\alpha_{g,i+1} \rho_{g,i+1} h_{0,i+1}^m$. The flux and pressure gradients are then calculated for cell i using the solution to the Riemann problem on each cell face that used γ_i . Since $\alpha_g \rho_g h_0^m$ is frozen, the quantity $\alpha_g \rho_g u_g h_0^m$ is not added to the energy flux. A requirement for the double-flux model is that the flux evaluation method preserves a stationary contact surface. HLLC (Harten *et al.* 1983; Toro *et al.* 1994) and AUSM (Liou 2006) meet this condition and the additional condition, mentioned in § 4.1, that the pressure is not directly included in momentum flux.

The double-flux model requires that the Riemann problem be calculated twice at each cell edge to give $\mathbf{R}_{g,i+1/2}^-$ and $\mathbf{R}_{g,i+1/2}^+$. This is the reason for separating the edge-centred variables with superscripts $+$ and $-$ in (B 1)–(B 8). The value of $\mathbf{R}_{g,i+1/2}^-$ is

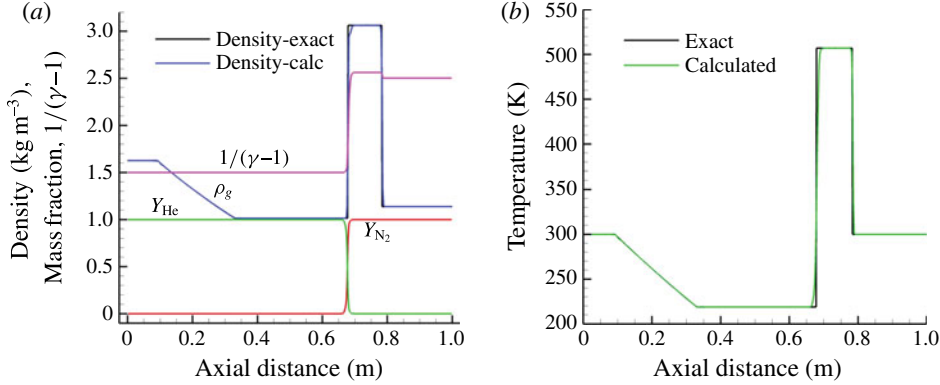


FIGURE 20. (Colour online) Comparison of the exact and computed solutions to the helium–nitrogen Riemann problem using the double-flux model with 400 points at a time of 400 μ s. The initial discontinuity was placed at $x=0.5$ m and the pressure of the pure He on the left was 10 atm and the pressure of the pure N₂ on the right was 1 atm. The temperature of both fluids was initially 300 K.

calculated from the interpolated primitive variables and HLLC with γ_i ; and $R_{g,i+1/2}^+$ is calculated from the same interpolated primitive variables, but using HLLC with γ_{i+1} .

The double-flux model is currently one of the only methods that can converge to the correct weak solution of multicomponent Riemann problems, as shown in figure 20. This problem models a shock tube where helium is placed on the driver side at 10 atm and 300 K. Nitrogen at 1 atm and 300 K is placed on the driven side of the shock tube. At $t=0$, the barrier separating the two gases is burst, and a shock propagates into the nitrogen and an expansion wave propagates into the helium. As shown in figure 20, the strengths and speeds of the shock and rarefaction waves compare well with the exact solution.

B.4. Granular flux evaluation

The AUSM⁺-up flux of Liou (2006) at computational cell edge $i+1/2$ is

$$\mathbf{F}_{s,i+1/2} = \mathbf{p}_{i+1/2} + \dot{m}_{s,i+1/2} \begin{cases} \boldsymbol{\psi}^L & \text{if } \dot{m}_{s,i+1/2} > 0, \\ \boldsymbol{\psi}^R & \text{if } \dot{m}_{s,i+1/2} \leq 0, \end{cases} \quad (\text{B } 20)$$

where $\mathbf{p}_{i+1/2}$ is a pressure flux vector that is non-zero only for the momentum equation, $\mathbf{p}_{i+1/2} = (0, 0, p_{s,tot,i+1/2}, 0, 0)^T$ and $\boldsymbol{\psi}$ is the vector of the passively advected scalars, $\boldsymbol{\psi} = (1, Y_{s,j}, u_s, E_s, e_s)^T$. The mass flux at the cell interface, modified slightly to avoid problems with hyperbolic degeneracy and to add dissipation as the packing limit is approached ($\alpha_s \rightarrow \alpha_{s,max}$), is defined by

$$\dot{m}_{s,i+1/2} = \mathcal{F} + c_{1/2} M_{1/2} \begin{cases} \alpha_s^L \rho_s^L & \text{if } M_{1/2} > 0, \\ \alpha_s^R \rho_s^R & \text{if } M_{1/2} \leq 0. \end{cases} \quad (\text{B } 21)$$

Here $M_{1/2}$ is the Mach number of the granular phase based on the compaction wave speed at the cell edge, defined below; \mathcal{F} is an extra dissipation term developed to

stabilize calculations where the packing limit is approached and friction pressure and compaction wave speed become extremely sensitive to minute volume-fraction fluctuations. It was found through numerical experimentation that \mathcal{F} with a functional form similar to the dissipation term for the Rusanov flux (Toro 1999) suppresses these oscillations,

$$\mathcal{F} = \frac{(c_{1/2} - \epsilon)[1 + |M_{1/2}|(1 - \mathcal{G}/2)] \max(\alpha_s^L, \alpha_s^R)}{2 \alpha_{s,max}} [\alpha_s^L \rho_s^L - \alpha_s^R \rho_s^R], \quad (\text{B } 22)$$

where $\alpha_{s,max}$ is the packing limit and \mathcal{G} is a dissipation-controlling parameter determined while interpolating the granular primitive variables (α_s , $Y_{s,i}$, \mathbf{v}_s , Θ_s , T_s) at edge $i + 1/2$ discussed below. The parameter ϵ is a small number (10^{-10}) to avoid division by zero when the compaction wave speed is zero. Note that the small parameter ϵ was unchanged in all of the numerical experiments presented in this paper.

The primitive variables for the granular phase are initially reconstructed using fifth-order symmetric bandwidth-optimized WENO (Martín *et al.* 2006) with nonlinear error controls (Taylor *et al.* 2007). The WENO-interpolated variables are then processed through a TVD slope limiter. The final interpolation for a slope-limited granular-phase variable Q is

$$Q_{i+1/2}^L = Q_i + 0.5(Q_i - Q_{i-1})\phi_{TVD}, \quad (\text{B } 23)$$

where ϕ_{TVD} is the slope limiter. The TVD slope limiter used in this work is from Houim & Kuo (2011) and Kim & Kim (2005),

$$\phi_{TVD} = \max \left[0, \min \left(\mathcal{G}, \mathcal{G} \frac{Q_{i+1} - Q_i}{Q_i - Q_{i-1}}, 2 \frac{\hat{Q}_{i+1/2}^L - Q_i}{Q_i - Q_{i-1}} \right) \right], \quad (\text{B } 24)$$

where $\hat{Q}_{i+1/2}^L$ is the original left-biased interpolated variable using WENO and

$$\mathcal{G} = \max[2(1 - \mathcal{D}\zeta^2), 0]. \quad (\text{B } 25)$$

Here $\mathcal{D} \geq 0$ is a user-defined constant that is set to 1 unless otherwise noted. The α_s^M is the maximum solid volume fraction in the entire stencil used by WENO for both left- and right-biased interpolations, and

$$\zeta = \begin{cases} \frac{\alpha_s^M - \alpha_{s,crit}}{\alpha_{s,max} - \alpha_{s,crit}} & \text{if } \alpha_s^M > \alpha_{s,crit}, \\ 0 & \text{if } \alpha_s^M < \alpha_{s,crit}, \end{cases} \quad (\text{B } 26)$$

where $\alpha_{s,crit}$ and $\alpha_{s,max}$ are the critical volume fraction and packing limit (see (3.22) and (3.23)). The form of \mathcal{G} and \mathcal{F} work well in dense granular regions to suppress oscillations, has relatively little influence on regions at low particle concentration, and does not interfere with the ability of AUSM⁺-up to capture stationary granular contact surfaces.

The effect of \mathcal{D} is twofold. First, it degrades the edge reconstruction scheme for the granular phase to first-order in dense regions. Second, \mathcal{D} explicitly increases the dissipation of AUSM⁺-up. The particular form of \mathcal{G} is chosen such that the transition

is smooth between regions of low volume fraction (where $\mathcal{G} = 2$) and high volume fraction (where $\mathcal{G} = 0$). Increasing \mathcal{D} increases the rate at which \mathcal{G} transitions from 2 to 0 as a function of α_s . Setting $\mathcal{D} = 1$ was found to work well in most cases, as shown in figures 8 and 9.

The averaged compaction wave speed needed for equation (B 21) is estimated by

$$c_{1/2} = \sqrt{\frac{\alpha_s^L \rho_s^L (c_s^L)^2 + \alpha_s^R \rho_s^R (c_s^R)^2}{\alpha_s^L \rho_s^L + \alpha_s^R \rho_s^R}} + \epsilon. \quad (\text{B } 27)$$

The averaged velocity is

$$u_{1/2} = c_{1/2} M_{1/2}, \quad (\text{B } 28)$$

where the split Mach number for the granular phase is computed by

$$M_{1/2} = \mathcal{M}_4^+(M^L) + \mathcal{M}_4^-(M^R) - 2 \frac{K_p}{f_a} \max(1 - \sigma \bar{M}^2, 0) \frac{p_{s,tot}^R - p_{s,tot}^L}{(\alpha_s^L \rho_s^L + \alpha_s^R \rho_s^R + \epsilon) c_{1/2}^2}, \quad (\text{B } 29)$$

with $f_a = 1$; K_p and σ are the AUSM dissipation parameters discussed below and

$$M^L = \frac{u_s^L}{c_{1/2}}, \quad M^R = \frac{u_s^R}{c_{1/2}}, \quad \bar{M}^2 = \frac{(u_s^L)^2 + (u_s^R)^2}{2c_{1/2}^2}. \quad (\text{B } 30a-c)$$

The split pressure at the cell face is

$$\begin{aligned} p_{s,tot,i+1/2} = & -K_u f_a (c_{1/2} - \epsilon) \mathcal{P}_5^+(M^L) \mathcal{P}_5^-(M^R) (\alpha_s^L \rho_s^L + \alpha_s^R \rho_s^R) (u_s^R - u_s^L) \\ & + \mathcal{P}_5^+(M^L) p_{s,tot}^L + \mathcal{P}_5^-(M^R) p_{s,tot}^R, \end{aligned} \quad (\text{B } 31)$$

where K_u is another AUSM dissipation parameter. Note that the value of ϵ must be identical in (B 22), (B 27) and (B 31) to compute accurate fluxes in the hyperbolically degenerate regions. The ϵ in (B 29) is to avoid division by zero when the bulk density of the granular phase is zero.

The pressure and Mach-number splitting polynomials needed to compute the AUSM flux are

$$\mathcal{M}_1^\pm(M) = \frac{1}{2}(M \pm |M|), \quad (\text{B } 32)$$

$$\mathcal{M}_2^\pm(M) = \pm \frac{1}{4}(M \pm 1)^2, \quad (\text{B } 33)$$

$$\mathcal{M}_4^\pm(M) = \begin{cases} \mathcal{M}_1^\pm(M) & \text{if } |M| \geq 1, \\ \mathcal{M}_2^\pm(M)[1 \mp 16\beta \mathcal{M}_2^\mp(M)] & \text{if } |M| < 1, \end{cases} \quad (\text{B } 34)$$

$$\mathcal{P}_5^\pm(M) = \begin{cases} \mathcal{M}_1^\pm(M)/M & \text{if } |M| \geq 1, \\ \mathcal{M}_2^\pm(M)[(\pm 2 - M) \mp 16\xi M \mathcal{M}_2^\mp(M)] & \text{if } |M| < 1, \end{cases} \quad (\text{B } 35)$$

where $\beta = 0.125$ and ξ is defined by

$$\xi = \frac{3}{16}(-4 + 5f_a^2). \quad (\text{B } 36)$$

The AUSM dissipation parameters are determined from \mathcal{G} by

$$K_p = 0.25 + 0.75(1 - \mathcal{G}/2), \quad (\text{B } 37)$$

$$K_u = 0.75 + 0.25(1 - \mathcal{G}/2), \quad (\text{B } 38)$$

$$\sigma = 0.75\mathcal{G}/2. \quad (\text{B } 39)$$

Finally, the gas-phase volume fraction at the cell edge is computed by

$$\alpha_{g,i+1/2} = \begin{cases} \alpha_{g,i+1/2}^L & \text{if } \dot{m}_{s,i+1/2} > 0, \\ \alpha_{g,i+1/2}^R & \text{if } \dot{m}_{s,i+1/2} \leq 0, \end{cases} \quad (\text{B } 40)$$

and the parameters needed for the non-conservative terms at the cell edge are

$$\alpha_{s,i+1/2} u_{s,i+1/2} = \begin{cases} \dot{m}_{s,i+1/2} / \rho_{s,i+1/2}^L & \text{if } \dot{m}_{s,i+1/2} > 0, \\ \dot{m}_{s,i+1/2} / \rho_{s,i+1/2}^R & \text{if } \dot{m}_{s,i+1/2} \leq 0, \end{cases} \quad (\text{B } 41)$$

$$u_{s,i+1/2} = \begin{cases} \dot{m}_{s,i+1/2} / \alpha_{s,i+1/2}^L \rho_{s,i+1/2}^L & \text{if } \dot{m}_{s,i+1/2} > 0, \\ \dot{m}_{s,i+1/2} / \alpha_{s,i+1/2}^R \rho_{s,i+1/2}^R & \text{if } \dot{m}_{s,i+1/2} \leq 0. \end{cases} \quad (\text{B } 42)$$

This modified AUSM⁺-up scheme for the granular phase reduces to the unmodified scheme if $\mathcal{F} = 0$, $\mathcal{G} = 2$ and $\epsilon = 0$. The small number, ϵ , is inserted into (B 21), (B 29) and (B 30a–c), but not the others, to produce a properly upwinded flux when $c_{1/2} = 0$ by cancelling the ϵ used to compute $c_{1/2}$ and $M_{1/2}$. In the case of zero total intergranular stress, the parameter $c_{1/2} M_{1/2}$ reduces to

$$c_{1/2} M_{1/2} = \frac{\epsilon}{2} \left[\frac{u_s^L + |u_s^L|}{\epsilon} + \frac{u_s^R - |u_s^R|}{\epsilon} \right] = \begin{cases} u_s^L & \text{if } u_s^L \geq 0 \text{ and } u_s^R > 0, \\ u_s^R & \text{if } u_s^L < 0 \text{ and } u_s^R \leq 0, \\ u_s^L + u_s^R & \text{if } u_s^L > 0 \text{ and } u_s^R < 0, \\ 0 & \text{if } u_s^L < 0 \text{ and } u_s^R > 0, \end{cases} \quad (\text{B } 43)$$

which, when combined with (B 20) and (B 21), produces a flux that is similar to the pressureless Riemann solver of Collins *et al.* (1994). This indicates that the modification to AUSM provides a proper upwinded flux even when the intergranular stress is zero.

B.5. Step-by-step solution procedure for the hyperbolic terms

The solution method for the hyperbolic terms for advancing the conserved variables from time level n to $n + 1$ for a multistage explicit integration method can be summarized as follows.

- (1) Calculate and store γ and $\alpha_g \rho_g h_0^m$ at each cell.
- (2) Compute the solutions to the gas and granular Riemann problems at each cell edge for each direction.
 - (a) Interpolate the granular-phase primitive variables (α_s , $Y_{s,j}$, u_s , Θ_s , T_s) from the left and right.
 - (i) Compute ζ from (B 26).
 - (ii) Compute \mathcal{G} from (B 25).
 - (iii) Interpolate the primitive variables. We use the six-point bandwidth-optimized WENO method of Martín *et al.* (2006) and Taylor *et al.* (2007).
 - (iv) Apply the slope limiter to the WENO-interpolated granular primitive variables using (B 23).
 - (v) Compute the total intergranular stress $p_{s,tot}$, E_s and e_s for the left- and right-reconstructed states.

- (b) Interpolate the gas-phase primitive variables ($Y_{g,j}, p_g, T_g, u_g$) to the cell face from the left and right. In this work we use the scheme given in Houim & Kuo (2011).
- (c) Solve the granular-phase Riemann problem using the modified AUSM⁺-up scheme. Store the $u_{s,i+1/2}$, $\alpha_{s,i+1/2}u_{s,i+1/2}$ and $\alpha_{g,i+1/2}$ in addition to the granular fluxes (see (4.14)–(4.16)).
- (d) Solve the gas-phase Riemann problem at each cell edge twice using the HLLC method detailed in § 3.1 to get $P_{g,i+1/2}^+$ and $P_{g,i+1/2}^-$. Rotate the HLLC solver near shocks using the method outlined in Houim & Kuo (2011) to avoid shock anomalies.
- (3) Compute the lift force (f_{Lift}) from (3.40) at each cell centre using second-order finite differences if $\alpha_s > \alpha_{s,min}$ for all points in the stencil where $\alpha_{s,min} = 10^{-10}$.
- (4) Assemble the right-hand side to discretize the convective terms and gravitational acceleration, (B 1)–(B 8).
- (5) Update the conserved variables, U_g and U_s , using the fully assembled right-hand side of the hyperbolic operator and the chosen time-marching method. We use the third-order strong-stability-preserving Runge–Kutta scheme (Spiteri & Ruuth 2003).
- (6) Update the gas-phase primitive variables in a manner consistent with the double-flux model via

$$\left. \begin{aligned} Y_{g,j} &= \frac{\alpha_g \rho_g Y_{g,j}}{\sum \alpha_g \rho_g Y_{g,j}}, & u_g &= \frac{\alpha_g \rho_g u_g}{\sum \alpha_g \rho_g Y_{g,j}}, & T_g &= \frac{p_g}{R_u \sum \frac{\rho_g Y_{g,j}}{M_j}}, \\ p_g &= \frac{\gamma^n - 1}{\alpha_g} \left[\alpha_g \rho_g E_g - (\alpha_g \rho_g h_0^m)^n - \alpha_g \rho_g \frac{\mathbf{v}_g \cdot \mathbf{v}_g}{2} \right]. \end{aligned} \right\} \quad (\text{B } 44)$$

- (7) Repeat steps 2–6 for each stage of the time-marching algorithm.
- (8) Use the granular-phase conserved variables, gas-phase primitive variables, gaseous species densities ($\alpha_g \rho_g Y_{g,j}$) and momenta calculated from the final stage of the time-stepping algorithm as values for the next time step, $n + 1$, and use them to calculate γ^{n+1} and $(\alpha_g \rho_g h_0^m)^{n+1}$.
- (9) Perform the final step of the double-flux method to update the total gas-phase energy for time step $n + 1$,

$$(\alpha_g \rho_g E_g)^{n+1} = \frac{\alpha_g^{n+1} p_g^{n+1}}{\gamma^{n+1} - 1} + (\alpha_g \rho_g h_0^m)^{n+1} + \alpha_g^{n+1} \rho_g^{n+1} \frac{\mathbf{v}_g^{n+1} \cdot \mathbf{v}_g^{n+1}}{2}. \quad (\text{B } 45)$$

- (10) Check for computational cells with very low particle volume fractions. If $\alpha_s < \alpha_{s,min}$, where $\alpha_{s,min} = 10^{-10}$, remove the granular phase and scale the gas-phase conserved variables to account for gas-phase volume gained by removal of the particulate phase: $U_g^{n+1} = U_g^{n+1} / (1 - \alpha_s^{n+1})$ and $U_s^{n+1} = 0$ if $\alpha_s^{n+1} < \alpha_{s,min}$.

If the double-flux model is not used, step 9 is unnecessary, step 2(d) would be completed using a single solution to the Riemann problem, and the primitive variables in step 6 would be determined using the actual gas-phase equation of state.

B.6. Solution of the source terms

Neglecting phase changes and chemical reactions, the remaining non-zero inhomogeneous source terms are

$$\frac{d\alpha_g \rho_g \mathbf{v}_g}{dt} = \mathbf{f}_{Drag}, \quad (\text{B } 46)$$

$$\frac{d\alpha_g \rho_g E_g}{dt} = -q_{conv} + \mathbf{f}_{Drag} \cdot \mathbf{v}_s + \phi_{visc} - \phi_{slip}, \quad (\text{B } 47)$$

$$\frac{d\alpha_s \rho_s \mathbf{v}_s}{dt} = -\mathbf{f}_{Drag}, \quad (\text{B } 48)$$

$$\frac{d\alpha_s \rho_s E_s}{dt} = -\dot{\gamma} - \phi_{visc} + \phi_{slip}, \quad (\text{B } 49)$$

$$\frac{d\alpha_s \rho_s e_s}{dt} = q_{conv} + \dot{\gamma}. \quad (\text{B } 50)$$

For each equation, the source terms are split into several substeps due to the wide variety of time scales between convection, drag, granular cooling ($\dot{\gamma}$), etc. A Strang splitting method is used,

$$\mathcal{S}^{2\Delta t} = \mathcal{S}_{qD}^{\Delta t}(\mathcal{S}_{\Theta}^{\Delta t}(\mathcal{S}_{\Theta}^{\Delta t}(\mathcal{S}_{qD}^{\Delta t}(\mathbf{U}^H)))), \quad (\text{B } 51)$$

where \mathbf{U}^H represents the conservative variable vector after the solution of the hyperbolic terms in the step of (4.1), $\mathcal{S}_{qD}^{\Delta t}$ advances the drag and convective heat transfer, and $\mathcal{S}_{\Theta}^{\Delta t}$ is the advancement of ϕ_{slip} , ϕ_{visc} and $\dot{\gamma}$.

B.7. Solution of the drag, and convective heat transfer terms

Considering only drag and heat transfer, the equations are

$$\frac{d\alpha_g \rho_g \mathbf{v}_g}{dt} = \mathbf{f}_{Drag}, \quad \frac{d\alpha_s \rho_s \mathbf{v}_s}{dt} = -\mathbf{f}_{Drag}, \quad (\text{B } 52a,b)$$

$$\frac{d\alpha_g \rho_g E_g}{dt} = -q_{conv} + \mathbf{f}_{Drag} \cdot \mathbf{v}_s, \quad \frac{d\alpha_s \rho_s e_s}{dt} = q_{conv}. \quad (\text{B } 53a,b)$$

If the drag and heat transfer coefficients and specific heats are evaluated using the initial conditions (parameters denoted with a superscript 0) and frozen during the integration, the drag and heat transfer terms can be integrated analytically (Pelanti & LeVeque 2006). Then the change in momentum from drag, $\Delta \mathbf{M}$, is

$$\Delta \mathbf{M} = \frac{\mathbf{v}_g^0 - \mathbf{v}_s^0}{\xi_D} \left[\frac{1}{K_{sg} \xi_D \Delta t + 1} - 1 \right], \quad (\text{B } 54)$$

where

$$\xi_D = \frac{1}{\alpha_g \rho_g} + \frac{1}{\alpha_s \rho_s}. \quad (\text{B } 55)$$

The change in internal energy from convection, Δe , is

$$\Delta e = \frac{T_g^0 - T_s^0}{\xi_e} \left[\exp \left(-6 \frac{\alpha_s \lambda_g Nu}{d_s^2} \xi_e \Delta t \right) - 1 \right], \quad (\text{B } 56)$$

where

$$\xi_e = \frac{1}{\alpha_g \rho_g C_{V,g}^0} + \frac{1}{\alpha_s \rho_s C_{V,s}^0}. \quad (\text{B } 57)$$

Then the momentum and energies at $t = \Delta t$ are

$$(\alpha_g \rho_g \mathbf{v}_g)^{\Delta t} = (\alpha_g \rho_g \mathbf{v}_g)^0 + \Delta \mathbf{M}, \quad (\text{B } 58)$$

$$(\alpha_s \rho_s \mathbf{v}_s)^{\Delta t} = (\alpha_s \rho_s \mathbf{v}_s)^0 - \Delta \mathbf{M}, \quad (\text{B } 59)$$

$$(\alpha_g \rho_g E_g)^{\Delta t} = (\alpha_s \rho_s E_g)^0 + \Delta e - \frac{(\alpha_s \rho_s)^0}{2} [\mathbf{v}_s^{\Delta t} \cdot \mathbf{v}_s^{\Delta t} - \mathbf{v}_s^0 \cdot \mathbf{v}_s^0], \quad (\text{B } 60)$$

$$(\alpha_s \rho_s e_s)^{\Delta t} = (\alpha_s \rho_s e_s)^0 - \Delta e. \quad (\text{B } 61)$$

B.7.1. Solution for pseudo-thermal energy production and dissipation

The ordinary differential equations for the source terms considering only sources and sinks of PTE are

$$\frac{d\alpha_g \rho_g E_g}{dt} = \phi_{visc} - \phi_{slip}, \quad (\text{B } 62)$$

$$\frac{d\alpha_s \rho_s E_s}{dt} = -\dot{\gamma} - \phi_{visc} + \phi_{slip}, \quad (\text{B } 63)$$

$$\frac{d\alpha_s \rho_s e_s}{dt} = \dot{\gamma}. \quad (\text{B } 64)$$

A predictor–corrector approach is used to integrate these terms independently, so that analytic solutions can be used. This is especially useful when the granular temperature is zero and ϕ_{slip} is singular, but analytically integrable. First, the dissipation of E_s from viscous damping is computed,

$$\Theta_s^* = \Theta_s^0 \exp \left[\frac{-2K_{sg} \Delta t}{\alpha_s \rho_s} \right]. \quad (\text{B } 65)$$

Next the production of PTE from velocity slip is integrated,

$$\Theta_s^{**} = \left[\frac{\xi_{slip}}{\alpha_s \rho_s} \Delta t + (\Theta_s^*)^{3/2} \right]^{2/3}, \quad (\text{B } 66)$$

where

$$\xi_{slip} = \frac{81\alpha_s \mu_g^2}{g_0 d_s^3 \rho_s \sqrt{\pi}} \frac{|\mathbf{v}_g^0 - \mathbf{v}_s^0|^2}{K_{sg} \xi_D \Delta t + 1}. \quad (\text{B } 67)$$

The factor $1/(K_{sg} \xi_D \Delta t + 1)$ in (B 67) comes from averaging $|\mathbf{v}_g^0 - \mathbf{v}_s^0|^2$ during particle acceleration from drag. Finally, dissipation of E_s due to inelastic granular collisions is integrated,

$$\Theta_s^{\Delta t} = \Theta_s^{**} \frac{9(\alpha_s \rho_s)^2}{[3\alpha_s \rho_s + \Delta t \xi_\gamma \sqrt{\Theta_s^{**}}]^2}, \quad (\text{B } 68)$$

where

$$\xi_\gamma = 12(1 - e^2)g_0 \alpha_s^2 \frac{\rho_s}{d_s \sqrt{\pi}}. \quad (\text{B } 69)$$

With the final and intermediate granular temperatures known, the energies after the time step are

$$(\alpha_s \rho_s E_s)^{\Delta t} = \frac{3}{2} (\alpha_s \rho_s)^0 \Theta_s^{\Delta t}, \quad (\text{B } 70)$$

$$(\alpha_s \rho_s e_s)^{\Delta t} = (\alpha_s \rho_s e_s)^0 - \frac{3}{2} (\alpha_s \rho_s)^0 (\Theta_s^{\Delta t} - \Theta_s^{**}), \quad (\text{B } 71)$$

$$(\alpha_g \rho_g E_g)^{\Delta t} = (\alpha_g \rho_g E_g)^{\Delta t} - \frac{3}{2} (\alpha_s \rho_s)^0 (\Theta_s^{**} - \Theta_s^0). \quad (\text{B } 72)$$

The integration order of the above three steps are reversed with each call to $\mathcal{S}_{\Theta}^{\Delta t}$. On a second call, $\dot{\gamma}$ is integrated first, followed by ϕ_{slip} , and then ϕ_{visc} .

REFERENCES

- ABGRALL, R. & KARNI, S. 2010 A comment on the computation of non-conservative products. *J. Comput. Phys.* **229** (8), 2759–2763.
- AGRAWAL, K., LOEZOS, P. N., SYAMLAL, M. & SUNDARESAN, S. 2001 The role of meso-scale structures in rapid gas–solid flows. *J. Fluid Mech.* **445** (1), 151–185.
- ANDREOTTI, B., FORTERRE, Y. & POULIQUEN, O. 2013 *Granular Media: Between Fluid and Solid*. Cambridge University Press.
- ASC FLASH Center 2012 *Flash User's Guide*. University of Chicago.
- BAER, M. R. & NUNZIATO, J. W. 1986 A two-phase mixture theory for the deflagration-to-detonation transition (DDT) in reactive granular materials. *Intl J. Multiphase Flow* **12** (6), 861–889.
- BALSARA, D. S. & SHU, C.-W. 2000 Monotonicity preserving weighted essentially non-oscillatory schemes with increasingly high order of accuracy. *J. Comput. Phys.* **160** (2), 405–452.
- BENKIEWICZ, K. & HAYASHI, A. K. 2002 Aluminum dust ignition behind reflected shock wave: two-dimensional simulations. *Fluid Dyn. Res.* **30** (5), 269–292.
- BILLET, G. & ABGRALL, R. 2003 An adaptive shock-capturing algorithm for solving unsteady reactive flows. *Comput. Fluids* **32** (10), 1473–1495.
- BRILLIANTOV, N. V. & PÖSCHEL, T. 2004 *Kinetic Theory of Granular Gases*. Oxford University Press.
- CAPECELATRO, J. & DESJARDINS, O. 2013 An Euler–Lagrange strategy for simulating particle-laden flows. *J. Comput. Phys.* **238**, 1–31.
- CHANG, C.-H. & LIOU, M.-S. 2007 A robust and accurate approach to computing compressible multiphase flow: stratified flow model and AUSM⁺-up scheme. *J. Comput. Phys.* **225** (1), 840–873.
- CHUANJIE, Z., BAIQUAN, L., BINGYOU, J., QIAN, L. & YIDU, H. 2012 Simulation of dust lifting process induced by gas explosion disaster in underground coal mine. *Disaster Adv.* **5** (4), 1407–1413.
- COLELLA, P. & WOODWARD, P. R. 1984 The piecewise parabolic method (PPM) for gas-dynamical simulations. *J. Comput. Phys.* **54** (1), 174–201.
- COLLINS, J. P., FERGUSON, R. E., CHIEN, K., KUHL, A. L., KRISPIN, J. & GLAZ, H. M. 1994 Simulation of shock-induced dusty gas flows using various models. In *25th AIAA Fluid Dynamics Conference, Colorado Springs, CO*.
- CROCHET, M. W. & GONTHIER, K. A. 2013 Numerical investigation of a modified family of centered schemes applied to multiphase equations with nonconservative sources. *J. Comput. Phys.* **255**, 266–292.
- DACOMBE, P., POURKASHANIAN, M., WILLIAMS, A. & YAP, L. 1999 Combustion-induced fragmentation behavior of isolated coal particles. *Fuel* **78** (15), 1847–1857.
- DREW, D. A. & LAHEY, R. T. JR. 1987 The virtual mass and lift force on a sphere in rotating and straining inviscid flow. *Intl J. Multiphase Flow* **13** (1), 113–121.
- EDWARDS, J. C. & FORD, K. M. 1988 Model of coal dust explosion suppression by rock dust entrainment. *Tech. Rep.* RI 9206, US Department of the Interior, Bureau of Mines.
- EINFELDT, B., MUNZ, C. D., ROE, P. L. & SJÖGREEN, B. 1991 On Godunov-type methods near low densities. *J. Comput. Phys.* **92** (2), 273–295.

- FAN, B. C., CHEN, Z. H., JIANG, X. H. & LI, H. Z. 2007 Interaction of a shock wave with a loose dusty bulk layer. *Shock Waves* **16** (3), 179–187.
- FEDOROV, A. V. & FEDORCHENKO, I. A. 2010 Numerical simulation of shock wave propagation in a mixture of a gas and solid particles. *Combust. Explos. Shock Waves* **46** (5), 578–588.
- FEDOROV, A. V., KHARLAMOVA, Y. V. & KHMEL', T. A. 2007 Reflection of a shock wave in a dusty cloud. *Combust. Explos. Shock Waves* **43** (1), 104–113.
- GERBER, S., BEHRENDT, F. & OEVERMANN, M. 2010 An Eulerian modeling approach of wood gasification in a bubbling fluidized bed reactor using char as bed material. *Fuel* **89** (10), 2903–2917.
- GIDASPOW, D. 1994 *Multiphase Flow and Fluidization*. Academic.
- GOOS, E., BURCAT, A. & RUSNIC, B. 2010 Ideal gas thermochemical database with updates from active thermochemical tables. <http://garfield.chem.elte.hu/Burcat/burcat.html>.
- GRINSTEIN, F. F., MARGOLIN, L. G. & RIDER, W. J. 2007 *Implicit Large Eddy Simulation: Computing Turbulent Fluid Dynamics*. Cambridge University Press.
- GUNN, D. J. 1978 Transfer of heat of mass to particles in fixed and fluidized beds. *Intl J. Heat Mass Transfer* **21**, 467–476.
- HAFF, P. K. 1983 Grain flow as a fluid-mechanical phenomena. *J. Fluid Mech.* **134**, 401–430.
- HARTEN, A., LAX, P. D. & VAN LEER, B. 1983 On upstream differencing and Godunov-type schemes for hyperbolic conservation laws. *SIAM Rev.* **25** (1), 35–61.
- HELLAND, E., OCCELLI, R. & TADRIST, L. 2000 Numerical study of cluster formation in a gas–particle circulating fluidized bed. *Powder Technol.* **110** (3), 210–221.
- HORIO, M. & KUROKI, H. 1994 Three-dimensional flow visualization of dilutely dispersed solids in bubbling and circulating fluidized beds. *Chem. Engng Sci.* **49** (15), 2413–2421.
- HOUIM, R. W. & KUO, K. K. 2011 A low-dissipation and time-accurate method for compressible multi-component flow with variable specific heat ratios. *J. Comput. Phys.* **230** (23), 8527–8553.
- HOUIM, R. W. & ORAN, E. S. 2015a Numerical simulation of dilute and dense layered coal-dust explosions. *Proc. Combust. Inst.* **35** (2), 2083–2090.
- HOUIM, R. W. & ORAN, E. S. 2015b Structure and flame speed of dilute and dense layered coal-dust explosions. *J. Loss Prev. Process. Ind.* **36**, 214–222.
- HUANG, K., WU, H., YU, H. & YAN, D. 2011 Cures for numerical shock instability in HLLC solver. *Intl J. Numer. Meth. Fluids* **65**, 1026–1038.
- IGCI, Y., ANDREWS, A. T., SUNDARESAN, S., PANNALA, S. & O'BRIEN, T. 2008 Filtered two-fluid models for fluidized gas–particle suspensions. *AIChE J.* **54** (6), 1431–1448.
- ISHII, M. & HIBIKI, T. 2006 *Thermo-Fluid Dynamics of Two-Phase Flow*. Springer.
- JENIKE, A. W. 1987 A theory of flow of particulate solids in converging and diverging channels based on a conical yield function. *Powder Technol.* **50** (3), 229–236.
- JOHNSON, P. C. & JACKSON, R. 1987 Frictional–collisional constitutive relations for granular materials, with application to plane shearing. *J. Fluid Mech.* **176**, 67–93.
- JOP, P., FORTERRE, Y. & POULIQUEN, O. 2006 A constitutive law for dense granular flows. *Nature* **441** (7094), 727–730.
- KAMENETSKY, V., GOLDSSTEIN, A., SHAPIRO, M. & DEGANI, D. 2000 Evolution of a shock wave in a granular gas. *Phys. Fluids* **12**, 3036.
- KARNI, S. & HERNÁNDEZ-DUEÑAS, G. 2010 A hybrid algorithm for the Baer–Nunziato model using the Riemann invariants. *J. Sci. Comput.* **45** (1–3), 382–403.
- KHMEL', T. A. & FEDOROV, A. V. 2014a Description of dynamic processes in two-phase colliding media with the use of molecular-kinetic approaches. *Combust. Explos. Shock Waves* **50** (2), 196–207.
- KHMEL', T. A. & FEDOROV, A. V. 2014b Modeling of propagation of shock and detonation waves in dusty media with allowance for particle collisions. *Combust. Explos. Shock Waves* **50** (5), 547–555.
- KHMEL', T. & FEDOROV, A. 2015 Numerical simulation of dust dispersion using molecular-kinetic model for description of particle-to-particle collisions. *J. Loss Prev. Process. Ind.* **36**, 223–229.

- KIM, K. H. & KIM, C. 2005 Accurate, efficient and monotonic numerical methods for multi-dimensional compressible flows. Part II: multi-dimensional limiting process. *J. Comput. Phys.* **208** (2), 570–615.
- KOCH, D. L. & SANGANI, A. S. 1999 Particle pressure and marginal stability limits for a homogenous monodisperse gas fluidized bed: kinetic theory and numerical simulations. *J. Fluid Mech.* **400**, 229–263.
- KOO, J. H. & KUO, K. K. 1977 Transient combustion in granular propellant beds. Part I. Theoretical modeling and numerical solution of transient combustion processes in mobile granular propellant beds. *Tech. Rep.* DAAG 29-74-G-0116. US Army Research Office.
- KUHL, A. L., BELL, J. B. & BECKNER, V. E. 2010 Heterogeneous continuum model of aluminum particle combustion in explosions. *Combust. Explos. Shock Waves* **46** (4), 433–448.
- LEVEQUE, R. J. 2004 The dynamics of pressureless dust clouds and delta waves. *J. Hyperbolic Diff. Equ.* **1** (2), 315–327.
- LHUILIER, D., CHANG, C.-H. & THEOFANOUS, T. G. 2013 On the quest for a hyperbolic effective-field model of disperse flows. *J. Fluid Mech.* **731**, 184–194.
- LING, Y., HASELBACHER, A. & BALACHANDAR, S. 2011a Importance of unsteady contributions to force and heating for particles in compressible flows. Part 1: Modeling and analysis for shock-particle interaction. *Intl J. Multiphase Flow* **37** (9), 1026–1044.
- LING, Y., HASELBACHER, A. & BALACHANDAR, S. 2011b Importance of unsteady contributions to force and heating for particles in compressible flows. Part 2: Application to particle dispersal by blast waves. *Intl J. Multiphase Flow* **37** (9), 1013–1025.
- LING, Y., WAGNER, J. L., BERESH, S. J., KEARNEY, S. P. & BALACHANDAR, S. 2012 Interaction of a planar shock wave with a dense particle curtain: modeling and experiments. *Phys. Fluids* **24** (11), 113301.
- LIU, M. S., CHANG, C. H., NGUYEN, L. & THEOFANOUS, T. G. 2008 How to solve compressible multifluid equations: a simple, robust, and accurate method. *AIAA J.* **46** (9), 2345–2356.
- LIU, M.-S. 1996 A sequel to AUSM: AUSM⁺. *J. Comput. Phys.* **129** (2), 364–382.
- LIU, M. S. 2006 A sequel to AUSM, Part II: AUSM⁺-up for all speeds. *J. Comput. Phys.* **214** (1), 137–170.
- LIU, Q., HU, Y., BAI, C. & CHEN, M. 2013 Methane/coal dust/air explosions and their suppression by solid particle suppressing agents in a large-scale experimental tube. *J. Loss Prev. Process. Ind.* **26** (2), 310–316.
- LUN, C. K. K., SAVAGE, S. B., JEFFREY, D. J. & CHEPURNIY, N. 1984 Kinetic theories for granular flow: inelastic particles in Couette flow and slightly inelastic particles in a general flowfield. *J. Fluid Mech.* **140**, 223–256.
- MACNEICE, P., OLSON, K. M., MOBARRY, C., DE FAINCHEIN, R. & PACKER, C. 2000 PARAMESH: a parallel adaptive mesh refinement community toolkit. *Comput. Phys. Commun.* **126** (3), 330–354.
- MARKATOS, N. C. 1986 Modelling of two-phase transient flow and combustion of granular propellants. *Intl J. Multiphase Flow* **12** (6), 913–933.
- MARKATOS, N. C. & KIRKCALDY, D. 1983 Analysis and computation of three-dimensional, transient flow and combustion through granulated propellants. *Intl J. Heat Mass Transfer* **26** (7), 1037–1053.
- MARTÍN, M. P., TAYLOR, E. M., WU, M. & WEIRS, V. G. 2006 A bandwidth-optimized WENO scheme for the effective direct numerical simulation of compressible turbulence. *J. Comput. Phys.* **220** (1), 270–289.
- MIURA, H. & GLASS, I. I. 1982 On a dusty-gas shock tube. *Proc. R. Soc. Lond. A* **382** (1783), 373–388.
- NERI, A., ONGARO, T. E., MACEDONIO, G. & GIDASPOW, D. 2003 Multiparticle simulation of collapsing volcanic columns and pyroclastic flow. *J. Geophys. Res.* **108** (B4), 2202.
- NIGMATULIN, R. I. 1990 *Dynamics of Multiphase Media*, vol. 1. Taylor & Francis.

- NUSCA, M. J., HORST, A. W. & NEWILL, J. F. 2004 Multidimensional, two-phase simulations of notional telescoped ammunition propelling charge. *Tech. Rep.* ARL-TR-3306. US Army Research Laboratory.
- NUSSBAUM, J., HELLUY, P., HÉRARD, J.-M. & CARRIÈRE, A. 2006 Numerical simulations of gas–particle flows with combustion. *Flow Turbul. Combust.* **76**, 403–417.
- ORAN, E. S. & GAMEZO, V. N. 2007 Origins of the deflagration-to-detonation transition in gas-phase combustion. *Combust. Flame* **148** (1–2), 4–47.
- PANDOLFI, M. & D’AMBROSIO, D. 2001 Numerical instabilities in upwind methods: analysis and cures for the ‘carbuncle’ phenomenon. *J. Comput. Phys.* **166** (2), 271–301.
- PARMAR, M., HASELBACHER, A. & BALACHANDAR, S. 2010 Improved drag correlation for spheres and application to shock-tube experiments. *AIAA J.* **48** (6), 1273–1276.
- PELANTI, M. & LEVEQUE, R. J. 2006 High-resolution finite volume methods for dusty gas jets and plumes. *SIAM J. Sci. Comput.* **24**, 1335–1360.
- POLUDNENKO, A. Y. & ORAN, E. S. 2010 The interaction of high-speed turbulence with flames: global properties and internal flame structure. *Combust. Flame* **157** (5), 995–1011.
- POLUDNENKO, A. Y. & ORAN, E. S. 2011 The interaction of high-speed turbulence with flames: turbulent flame speed. *Combust. Flame* **158** (2), 301–326.
- PORTERIE, B. & LORAUD, J. C. 1994 An investigation of interior ballistics ignition phase. *Shock Waves* **4**, 81–93.
- ROGUE, X., RODRIGUEZ, G., HAAS, J. F. & SAUREL, R. 1998 Experimental and numerical investigation of the shock-induced fluidization of a particles bed. *Shock Waves* **8** (1), 29–45.
- SAITO, T., MARUMOTO, M. & TAKAYAMA, K. 2003 Numerical investigations of shock waves in gas–particle mixtures. *Shock Waves* **13** (4), 299–322.
- SAPKO, M. J., WEISS, E. S., CASHDOLLAR, K. L. & ZLOCHOWER, I. A. 2000 Experimental mine and laboratory dust explosion research at NIOSH. *J. Loss Prev. Process. Ind.* **13** (3–5), 229–242.
- SAUREL, R. & ABGRALL, R. 1999 A multiphase Godunov method for compressible multifluid and multiphase flows. *J. Comput. Phys.* **150** (2), 425–467.
- SCHNEIDERBAUER, S., AIGNER, A. & PIRKER, S. 2012 A comprehensive frictional–kinetic model for gas–particle flows: analysis of fluidized and moving bed regimes. *Chem. Engng Sci.* **80** (1), 279–292.
- SCHWENDEMAN, D. W., WAHLE, C. W. & KAPILA, A. K. 2006 The Riemann problem and a high-resolution Godunov method for a model of compressible two-phase flow. *J. Comput. Phys.* **212** (2), 490–526.
- SERNA, S. & MARQUINA, A. 2005 Capturing shock waves in inelastic granular gases. *J. Comput. Phys.* **209** (2), 787–795.
- SPITERI, R. J. & RUUTH, S. J. 2003 A new class of optimal high-order strong-stability-preserving time discretization methods. *SIAM J. Numer. Anal.* **40** (2), 469–491.
- SRIVASTAVA, A. & SUNDARESAN, S. 2003 Analysis of a frictional–kinetic model for gas–particle flow. *Powder Technol.* **129** (1), 72–85.
- SYAMLAL, M., ROGERS, W. & O’BRIEN, T. J. 1993 *MFIX Documentation*, Vol. 1, *Theory Guide*. Tech. Rep. DOE/METC-9411004, NTIS/DE9400087. National Technical Information Service.
- TALBOT, L., CHENG, R. K., SCHEFER, R. W. & WILLIS, D. R. 1980 Thermophoresis of particles in a heated boundary layer. *J. Fluid Mech.* **101** (4), 737–758.
- TAYLOR, E. M., WU, M. & MARTÍN, M. P. 2007 Optimization of nonlinear error for weighted essentially non-oscillatory methods in direct numerical simulations of compressible turbulence. *J. Comput. Phys.* **223** (1), 384–397.
- THORNBUR, B., MOSEDALE, A. & DRIKAKIS, D. 2007 On the implicit large eddy simulations of homogeneous decaying turbulence. *J. Comput. Phys.* **226** (2), 1202–1299.
- THORNBUR, B., MOSEDALE, A., DRIKAKIS, D., YOUNGS, D. & WILLIAMS, R. J. R. 2008 An improved reconstruction method for compressible flows with low Mach number features. *J. Comput. Phys.* **227** (10), 4873–4894.

- TORO, E. F. 1989 Riemann-problem-based techniques for computing reactive two-phased flows. In *Numerical Combustion* (ed. Dervieux A. & Larrouturou B.), Lecture Notes in Physics, vol. 351, pp. 472–481. Springer.
- TORO, E. F. 1999 *Riemann Solvers and Numerical Methods for Fluid Dynamics*, 2nd edn. Springer.
- TORO, E. F., SPRUCE, M. & SPEARES, W. 1994 Restoration of the contact surface in the HLL-Riemann solver. *Shock Waves* **4** (1), 25–34.
- VAN DER WEELE, K. 2008 Granular gas dynamics: how Maxwell's demon rules in a non-equilibrium system. *Contemp. Phys.* **49** (3), 157–178.
- VAN WACHEM, B. G. M., SCHOUTEN, J. C., VAN DEN BLEEK, C. M., KRISHNA, R. & SINCLAIR, J. L. 2001 Comparative analysis of CFD models of dense gas–solid systems. *AIChE J.* **47** (5), 1035–1051.
- WAGNER, J. L., BERESH, S. J., KEARNEY, S. P., TROTT, W. M., CASTANEDA, J. N., PRUETT, B. O. & BAER, M. R. 2012 A multiphase shock tube for shock wave interactions with dense particle fields. *Exp. Fluids* **52** (6), 1507–1517.
- WAYNE, P. J., VOROBIEFF, P., SMYTH, H., BERNARD, T., CORBIN, C., MALONEY, A., CONROY, J., WHITE, R., ANDERSON, M., KUMAR, S. *et al.* 2013 Shock-driven particle transport off smooth and rough surfaces. *Trans. ASME J. Fluids Engng* **135** (6), 061302.
- WILSON, L. 1980 Relationships between pressure, volatile content and ejecta velocity in three types of volcanic explosion. *J. Volcanol. Geotherm. Res.* **8** (2), 297–313.
- ZÈMERLI, C. 2013 Continuum mechanical modeling of dry granular systems: from dilute flow to solid-like behavior. PhD thesis, Technical University of Kaiserslautern.
- ZHANG, D. Z. 2005 Evolution of enduring contacts and stress relaxation in a dense granular medium. *Phys. Rev. E* **71**, 041303.
- ZHAO, Z. & FERNANDO, H. J. S. 2007 Numerical simulation of scour around pipelines using an Euler–Euler coupled two-phase model. *Environ. Fluid Mech.* **7** (2), 121–142.
- ZHENG, Y.-P., FENG, C.-G., JING, G.-X., QIAN, X.-M., LI, X.-J., LIU, Z.-Y. & HUANG, P. 2009 A statistical analysis of coal mine accidents caused by coal dust explosions in China. *J. Loss Prev. Process. Ind.* **22** (4), 528–532.
- ZHOU, W., ZHAO, C. S., DUAN, L. B., QU, C. R. & CHEN, X. P. 2011 Two-dimensional computational fluid dynamics simulation of coal combustion in a circulating fluidized bed combustor. *Chem. Engng J.* **166** (1), 306–314.
- ZIMMERMANN, S. & TAGHIPOUR, F. 2005 CFD modeling of the hydrodynamics and reaction kinetics of FCC fluidized-bed reactors. *Ind. Engng Chem. Res.* **44** (26), 9818–9827.
- ZYDAK, P. & KLEMENS, R. 2007 Modelling of dust lifting process behind propagating shock wave. *J. Loss Prev. Process. Ind.* **20** (4), 417–426.